



HAL
open science

Polarized observations for advanced atmosphere-ocean algorithms using airborne multi-spectral hyper-angular polarimetric imager

Ahmed El-Habashi, Jeffrey Bowles, Robert Foster, Deric Gray, Malik Chami

► **To cite this version:**

Ahmed El-Habashi, Jeffrey Bowles, Robert Foster, Deric Gray, Malik Chami. Polarized observations for advanced atmosphere-ocean algorithms using airborne multi-spectral hyper-angular polarimetric imager. *Journal of Quantitative Spectroscopy and Radiative Transfer*, 2021, 262 (March), pp.107515. 10.1016/j.jqsrt.2021.107515 . insu-03106714v2

HAL Id: insu-03106714

<https://insu.hal.science/insu-03106714v2>

Submitted on 28 Jan 2021

HAL is a multi-disciplinary open access archive for the deposit and dissemination of scientific research documents, whether they are published or not. The documents may come from teaching and research institutions in France or abroad, or from public or private research centers.

L'archive ouverte pluridisciplinaire **HAL**, est destinée au dépôt et à la diffusion de documents scientifiques de niveau recherche, publiés ou non, émanant des établissements d'enseignement et de recherche français ou étrangers, des laboratoires publics ou privés.



Distributed under a Creative Commons Attribution 4.0 International License



ELSEVIER

Contents lists available at ScienceDirect

Journal of Quantitative Spectroscopy & Radiative Transfer

journal homepage: www.elsevier.com/locate/jqsrt

Polarized observations for advanced atmosphere-ocean algorithms using airborne multi-spectral hyper-angular polarimetric imager



Ahmed El-Habashi^{a,b,*}, Jeffrey Bowles^a, Robert Foster^{a,b}, Deric Gray^a, Malik Chami^c

^a Remote Sensing Division, Naval Research Laboratory, Washington, DC20375, United States

^b National Research Council, Washington, DC, United States

^c Sorbonne Université, CNRS-INSU, Laboratoire Atmosphères Milieux Observations Spatiales (LATMOS), Boulevard de l'Observatoire, CS 34229, 06304 Nice Cedex, France

ARTICLE INFO

Article history:

Received 12 June 2020

Revised 28 December 2020

Accepted 6 January 2021

Available online 10 January 2021

Keywords:

Vector radiative transfer

Remote sensing

Polarimetry

VICO

PACE

Ocean Color

Retrieval algorithms

Open ocean

Coastal waters

Scattering

Bio-optics

Plankton

Chlorophyll-a

Minerals

CDOM

ABSTRACT

Airborne measurements of the linear polarization state of light were carried out over coastal and open ocean conditions to study aerosol and water column properties and investigate the possibility of using a multi-spectral, hyper-angular imaging polarimeter for retrieving aerosol and hydrosol optical properties. The instrument, the Versatile Imager for the Coastal Ocean (VICO), is used to support the analysis of ocean color polarized observations and their implication for future space-borne polarimetry such as the polarimeters planned to be deployed with the NASA Plankton, Aerosol, Cloud, and ocean Ecosystem (PACE) mission. Several sets of images at different viewing angles from the visible to the near-infrared spectrum were collected and compared with simulations using a vector radiative transfer (VRT) code. The simulations were obtained based on measured seawater inherent optical properties from shipborne instruments and measured atmospheric parameters from the Aerosol Robotic Network (AERONET) and a shipborne sunphotometer at different locations. An uncertainty method has been derived by propagating uncertainties from the measured polarized radiances. The method demonstrates practicable uncertainty formulations that can be used to construct a measurement uncertainty budget for the polarized data products. Results from VICO and the VRT simulation are consistent for both radiance and polarization spectrum at all the measured viewing angles. The total and polarized water-leaving reflectances are retrieved at four bands and varied geometries. It is also shown that the polarized remote sensing reflectance measured at various angles could be used to distinguish between the aerosols' and hydrosols' optical signatures by exploiting the fact that the polarized reflectance is fairly insensitive to hydrosols for given acquisition geometries. This study thus provides an opportunity to investigate various relationships between the microphysical properties of the oceanic and atmospheric particulates such as refractive index and particle size properties. It also contributes to the development of polarization-based inverse ocean color algorithms. Finally, the provided analysis gives insights for the validation of the ocean color parameters that will be retrieved from the forthcoming polarimetric satellite missions.

© 2021 The Authors. Published by Elsevier Ltd.

This is an open access article under the CC BY-NC-ND license (<http://creativecommons.org/licenses/by-nc-nd/4.0/>)

1. Introduction

Total and polarized light emerging from the atmosphere and oceans plays a significant role in the Earth's radiation budget. The objective of the field of ocean color (OC) is to provide accurate monitoring of oceanic optical properties and, using remote sensing instrumentation, understand what physical ocean constituents provide that signature. Conventional OC sensors are designed to mea-

sure the total radiances from below or above water, using shipborne, airborne, or space-borne platforms. The fundamental quantity derived from OC sensors is the spectral water-leaving radiance upwelling from below the ocean surface and passing through the ocean-air interface. The water-leaving radiance is determined by properties of the incident light and the scattering and absorption characteristics of the ocean water and its constituents. These scattering and absorption processes are best described by the inherent optical properties (IOPs) of the seawater. Overall, it is these IOPs that determine oceanic watercolor. The total radiance measured by a satellite sensor is principally controlled by the downwelling irradiance, the interactions of that light with the atmo-

* Corresponding author.

E-mail address: ahmed.el-habashi.ctr@nrl.navy.mil (M. Chami).

sphere, the air-ocean boundary, and the water constituents. To accurately determine water IOPs, and from them water constituents, it is first necessary to compute water-leaving radiance correctly. To do so from satellite observations, identifying and removing the non-water leaving contributions to the Top of Atmosphere (TOA) radiance is essential. This is the goal of atmospheric correction (AC) techniques. Various AC methods [1,2], along with empirical and semi-analytical IOP retrieval algorithms [3-11] were developed, to obtain the water optical properties and to retrieve the IOPs of the water constituents from TOA total radiance measurements. However, this process is still challenging in coastal waters where the aerosols can be strongly absorbing due to, black carbon, brown carbon, and/or mineral dust from the nearby cities. This condition is particularly true where atmospheric correction methods do not work well for the 400-470 wavelengths, which are strongly affected by the blue sky background signal [12,13]. Consequently, algorithms that rely on satellite measurements at these wavelengths to retrieve IOPs are vulnerable to retrieval inaccuracies [12]. Additionally, coastal waters exhibit overlapping absorption spectra between water constituents, as well as non-covarying components and overlapping scattering spectra, making it difficult to separate individual components. The development of inverse ocean color algorithms requires an accurate retrieval of the water-leaving signal and the capability to determine the full characteristics of the aerosol and hydrosol particles. Advances in polarimetric remote sensing (PRS) provide both higher retrieval accuracy [14-16] and additional information on the determination of the optical and micro-physical properties of suspended particulates [17-19]. The use of PRS has been widely recognized as a critical tool for reliable characterization of aerosol and hydrosol parameters [20-22]. Several spaceborne and airborne sensors [23-26] were developed to measure the polarization state in addition to the scalar radiance measurements. PRS is expected to yield significant advances in ocean color.

The main objective of this work is to demonstrate the capabilities of an operational airborne multi-spectral hyper angular polarimetric imager, called Versatile Imager for the Coastal Ocean VICO [25], over open ocean and coastal water conditions. Optical closure between VICO and the vector radiative transfer (VRT) forward modeling was achieved based on actual measurements of aerosol and seawater optical properties obtained at two different locations. Results are informative, in comparison with the traditional total radiance imaging, suggesting further advancement of polarimetric retrieval over both open ocean and coastal waters should be a goal of the ocean color community. The organization of this paper is as follows: Section 2 provides a brief review of the advancement of aerosol and hydrosol polarimetry. Section 3 describes how the field measurements are analyzed, and the uncertainty methodology applied in this work. Section 4 describes the VRT modeling approaches. Results and discussions on VICO and the TOA observations with the VRT simulations at the different conditions are shown in Section 5. Finally, a summary of the results is presented in Section 6.

2. Polarimetric remote sensing

Over the last several decades, the development of ocean color instruments has been based on measurements of a single-view multi-spectral radiance of the visible light. The Coastal Zone Color Scanner Experiment (CZCS) was the first single-viewed ocean color instrument launched into space in 1978. Following the CZCS, a fleet of single-view satellite sensors such as SeaWiFS, MODIS, VIIRS, MERIS, OLCI, and GOCI was launched, providing a continuous data record of the global ocean over the past two decades. These single-view instrument were used to drive several standard

ocean color products such as surface concentrations and the inherent optical properties of the different water constituents. In 1999, the Multi-angle Imaging SpectroRadiometer (MISR) was launched to observe Earth's climate with cameras pointed at nine different angles. MISR was designed to improve our understanding of the amount of sunlight scattered in different directions by the Earth's atmosphere, ocean, land, snow, and ice. The developed single-view and multi-view instruments utilize spectral radiance observations to drive several atmosphere-ocean products.

While these instruments provided a wealth of ocean color information, higher retrievals accuracy and additional products are needed for better characterization of the aerosol and hydrosol constituents. Polarimetry is well-suited to address these needs. Current and future planned remote sensing polarimeters can measure the degree of linear polarization to an absolute accuracy < 0.2%. The radiative transfer codes used to analyze these polarimetric measurements can provide an accuracy that exceeds state-of-the-art polarimeters < 0.2%. Chowdhary et al. [27] provided tabulated numerical reflectance values of the total and linearly polarized upwelling radiance just above a rough ocean surface, and at the top of the atmosphere (TOA) with high accuracy using three independent deterministic solutions of the radiative transfer. The tabulated reflectance values were within 10^{-5} - 10^{-6} of each other, for different viewing geometries, wavelengths, and atmosphere-ocean systems. The accuracy in the degree of linear polarization was less than 0.1% for most simulated cases and better than 0.2% overall. The agreements were validated through the use of stochastic (Monte Carlo) radiative transfer code. Similar agreements were achieved between the stochastic and probabilistic solutions of the vector radiative transfer. Regardless of the high accuracy achieved between the different VRT methods, it is important to note that the agreement here is a measure of how the model represent the physics of the different complex atmosphere-ocean systems, and does not necessarily mean that measurements of reality should be at the same level of accuracy.

Additionally, the polarized light field showed the capability of providing additional information on the micro-physical and macro-physical properties of aerosol and hydrosol particles, which are difficult to infer from the scalar scattered radiation observed by the current ocean color instruments [18,28,29]. Polarization is sensitive to the aerosol and hydrosol particles composition (complex refractive index), size, and shape. The polarized light reflected from the sea surface contains useful information on the sea state. It is expected that the polarized remote sensing will provide an accurate atmospheric correction that can lead to improved and new aerosol and hydrosol products [30,31].

2.1. Space-borne and airborne polarimeters

The first space-based polarimetric imagery was provided by the POLarization and Directionality of the Earth's Reflectance (POLDER) missions launched by the Centre National d'Etudes Spatiales (CNES) to provide accurate monitoring of aerosol properties [32-35]. POLDER-1 and 2, onboard the Advanced Earth Observing Satellite (ADEOS) 1 and 2, were launched in 1996 and 2002, respectively. Both POLDER missions ended prematurely within nearly a year due to host satellite communication failure with POLDER-1 and satellite's solar panel malfunctioned with POLDER-2. The longest record of space polarimetric observation was achieved by POLDER-3 onboard the Polarization and Anisotropy of Reflectances for Atmospheric Sciences coupled with Observations from a Lidar (PARASOL) platform with a lifespan of nine years (2004-2013). The polarimetric dataset from these instruments provided the most detailed global aerosol products, such as composition and micro-physic of the different aerosol types. Following POLDER, several space-borne and airborne polarimeters were flown by various na-

tional and international space agencies for better characterizations of Earth's atmosphere, ocean, and land. A brief summary of the current and planned polarimeters is given in the following paragraphs.

In 2011, the National Aeronautics and Space Administration (NASA) launched the Aerosol Polarimetry Sensor (APS) on the Glory mission [36,37]. The APS was designed to observe the out-going top-of-atmosphere (TOA) radiation at nine bands from visible to short wave infrared spectra at a spatial resolution of 5.6 km at nadir, and a swath of 5.6 km cross-track by 2200 km along-track. The linear polarization measurements were made at all wavelengths and from 250 viewing angles between $+60^\circ$ and -80° with respect to nadir. APS was expected to provide the most accurate data on the chemical, micro-physical, and optical properties of aerosols and their spatial and temporal distributions; unfortunately, the instrument did not successfully enter orbit due to a launch failure. In 2017, the Japan Aerospace Exploration Agency (JAXA) launched the Second Generation Global Imager (SGLI) onboard the Global Change Observation Mission-Climate (GCOM-C) [38]. The SGLI was designed to observe the out-going TOA radiation at 19 bands from near Ultra Violet (UV) to thermal infrared spectra at a spatial resolution of 250 m (1 km for the 763 nm band), and a swath of $\pm 45^\circ$ (1150 km). The linear polarization measurements are only available at two wavelengths (673.5 nm and 868.5 nm) at a spatial resolution of 1 km² and from one viewing angle, providing scattering angle directions between 60° and 120° . The Chinese Space Agency (CNSA) recently launched several polarimeters: the Multi-Angle Polarization Imager MAI [39] onboard the TianGong-2 (TG-2) spacecraft (2016), the Cloud and Aerosol Polarization Imager CAPI [40] onboard of the TanSat mission (2016), and the Directional Polarimetric Camera DPC [41] onboard the GaoFen-5 (GF5) spacecraft (2018). The MAI is an Earth observation instrument providing multi-channel multi-angle polarization measurements at six bands from visible to near-infrared at a spatial resolution of 3 km and a swath width of 770 km. The linear polarization measurements are only available at three wavelengths, centered at 565, 670, and 865 nm, and from 12 different viewing directions. The CAPI is a 5 bands imager from near ultra violet to short wave infrared spectra at a spatial resolution of 1 km and a swath of 400 km x 0.5 km. The linear polarization measurements are only available at two wavelengths (670 nm and 1640 nm) and from one viewing angle. The DPC has 8 channels from visible to near infrared at a spatial resolution of 3.3 km and a swath of 1850 km x 1850 km ($\pm 50^\circ$ across/along-track). The linear polarization measurements are available at 3 wavelengths, centered at 490, 670, and 865 nm, and from 9 different viewing directions.

To an increasing extent, several future missions are scheduled for launch all by 2023. The Multi-Angle Imager for Aerosols (MAIA) [42-44] planned to fly onboard of the Orbital Test Bed 2 (OTB-2) spacecraft as a part of the NASA Earth Venture Instrument program. MAIA is a targeted instrument capable of using a step-and-stare or sweep viewing mode over targeted areas. It is designed to observe targets at 14 bands from near-ultraviolet to thermal infrared spectra at a spatial resolution of about 200 m at nadir. The linear polarization measurements are available at three wavelengths, centered at 444, 646, and 1044 nm, and from typically 5-9 viewing angles in step-and-stare mode and continuously varying viewing angles in sweep mode. NASA plans to fly a hyperspectral imaging radiometer [45], the Ocean Color Instrument (OCI), and two polarimeters [46,47] the Hyper Angular Rainbow Polarimeter-2 (HARP2), and the Spectro-Polarimeter for Planetary Exploration (SPEXone) onboard of the Plankton, Aerosol, Cloud, and ocean Ecosystem (PACE) observatory [48]. HARP2 [49] was designed to observe the out-going TOA radiation at four wavelengths from visible to near-infrared spectra at a spatial resolution of 3 km and a wide swath of $\pm 47^\circ$ (1,556 km at nadir). The linear

polarization measurements are made at all bands and from 60 viewing angles for the 670 nm band and 20 viewing angles for other bands. HARP2 viewing angles are spaced over 114° . SPEXone [50] was designed to observe hyperspectral linear polarization from visible to near-infrared spectra at a spatial resolution of 4.6×5.4 km² and a narrow swath of $\pm 4^\circ$ (100 km at nadir). The linear polarization measurements are made at five viewing angles between $\pm 57^\circ$. The European Space Agency (ESA) planned to fly a hyperspectral imaging spectrometer, the Ultra-violet, Visible and Near-infrared Sounder (UVNS) and the Multi-View Multi-Channel Multi-Polarization Imaging (3MI) spectro-polarimeter onboard of the EUMETSAT Polar System -Second Generation (EPS-SG) as part of its Sentinel-5 space mission [51]. 3MI is the successor of POLDER satellite series. The instrument was designed to observe the out-going TOA radiation at 12 wavelengths from visible to far infrared spectra at a spatial resolution of 4 km² at nadir and a minimum swath of 2200 km. The linear polarization measurements are available at 9 wavelengths and at 10 to 14 viewing angles for any given target. The CNSA has approved to launch several space-borne polarimeters [20]: the Particulate Observing Scanning Polarimeter (POSP) onboard the Chinese Environmental Satellite-2 (HJ-2), the Synchronization Monitoring Atmospheric Corrector (SMAC) onboard the High-Resolution Multi-Mode satellite-1 (GFDM-1), the Polarization CrossFire Suite (PCF) onboard the GaoFen-5 spacecraft, and Directional Polarimetric Camera with polarized Lidar (DPC-Lidar) onboard the Carbon Monitoring satellite-1 (CM-1). The POSP is an all polarized scanning polarimeter with channels from near-UV to SWIR (410-2250 nm) at a spatial resolution of about 6 km and a wide swath of $\pm 32.5^\circ$. The POSP optical design closely follows the NASA APS. SMAC will provide linear polarization measurements at five wavelengths, centered at 490, 670, 870, 1610, and 2250 nm, with a spatial resolution of 7×8 km at two observing pixels along the cross-track direction. The PCF is a synergetic design of both the DPC and POSP instruments, which will allow a broad spectral and polarization range (380-2250nm) with at least 100 viewing directions in the angular range of $\pm 50^\circ$. The DPC-Lidar combines passive and active polarimetric measurements. It will provide DPC-like measurements with two spectral channel LIDAR centered at 532 (polarized) and 1064 nm. The National Academy of Sciences of Ukraine (NASU) planned to launch the Main Astronomical Observatory (MAO) by 2022 [52]. MAO is an all polarized scanning polarimeter with channel from near-UV to SWIR (370-1610 nm) at a spatial resolution of 6 km at nadir and a swath of $+50^\circ$ to -60° along track and $\pm 0.25^\circ$ across track.

Airborne polarimeters improve our ability to make polarimetric space measurements. They are developed to provide highly accurate calibrated observations that can be used to verify the space polarimeters concept and validate data processing and algorithms performance. The majority of the developed airborne polarimeters are designed as prototypes of current and planned orbital polarimeters. The MICROWavelength POLarimeter (MICROPOL)/the Observing System Including Polarisation (OSIRIS) [53-56], the Research Scanning Polarimeter (RSP) [14,17,21,57-59], the Airborne Multiangle Spectropolarimetric Imager (AirMSP1 and 2) [60-63], the Airborne SPEX [64,65], and the Airborne HARP (AirHARP), serve as the airborne prototypes for POLDER/3MI [32-35,66,67], APS [36,37], MAIA [42-44], SPEXone [50], and HARP2 [49] space instruments, respectively [20]. The expected polarimetric accuracies from these polarimeters are 2-3%, <0.2%, <1%, 0.3-0.5%, and 0.3-1% in the measured degree of linear polarization (DoLP), respectively. Most of these polarimetric accuracies are sufficient for several Earth's remote sensing applications. The current polarimetric applications are mainly focused on accurately characterizing aerosol and cloud optical and microphysical properties. However, an improved aerosol and cloud characterization results in better atmospheric corrections for the ocean color products and more accu-

rate retrievals of total and polarized water-leaving radiances. Several studies focused on developing joint retrieval algorithms that retrieve aerosol and water-leaving radiance using data from different multi-angle polarization measurements. Polarimetric datasets from the RSP [21,58,68], PARASOL [69], and AirMSPI [61] were used in combination with the coupled atmosphere-ocean simulations to retrieve the aerosol and hydrosol properties simultaneously. The developed algorithms used different aerosol and bio-optical models with different parameterizations for the joint retrievals. The concepts of the available and planned polarimeters, their technical designs, and the accompanying algorithm development are discussed in greater detail in Dubovik et al. (2019) [20].

2.2. Ocean color polarimetry

The characterization of hydrosol properties from polarimetric observations is limited. There has been only one study that used space sensors measurements [23] to show the potential of using polarization to distinguish hydrosols microphysical properties. Loisel et al. used POLDER observations and the radiative transfer simulations to show a hyperbolic trend between the scalar reflectance and the degree of linear polarization, which could be explained by changes in the bulk assemblages of the suspended marine particles. Nevertheless, several theoretical and in-situ based studies [15,24,29,70-79] have highlighted the importance of polarization in retrieving oceanic constituents. Kattawar et al. (2013) [29] provided a general review to understand the evolution of polarized light in the ocean and the role of polarization as a possible tool for underwater remote sensing. Chowdhary et al. [27] highlighted the ability to simulate and measure linear polarization signatures accurately and to allow for better characterization of the aerosol and hydrosol properties. Chami (2007) [15] has shown that polarized reflectance could efficiently retrieve the concentration of inorganic particles regardless of the phytoplankton content in coastal waters using an empirical-based inversion approach. Chami and Defoin-Platel (2007) [16] showed that the consideration of polarization within inverse algorithm leads to a much greater increase of the performance of the inversion, typically by a factor of 4 for the retrieval of the oceanic scattering coefficient. Tonizzo et al. (2011) [71] estimated particle composition and size distribution from simulated and in-situ measured polarized water-leaving radiance. Koestner et al. (2020) [80] examined diverse seawater samples from different coastal environments to provide a thorough characterization of the size distribution and composition of the marine particle with the angle-resolved polarized light scattering. Ibrahim et al. (2016) [74] retrieved the ratio of attenuation-to-absorption coefficients from the observed DoLP. Foster et al. (2016) [81] developed polarized transfer functions to determine the underwater polarized light field from above sea surface observations. El-Habashi et al. (2016, 2017, 2018) [76] were able to retrieve the sun-induced chlorophyll-a fluorescence, which is un-polarized, in a variety of oligotrophic and eutrophic waters utilizing the fractional reduction in the observed DoLP at the fluorescence region. Polarimetric measurements and vector radiative transfer (VRT) results are potentially promising for improved characterization of the aerosol and hydrosol particulates. They are expected to yield significant advances in OC retrieval algorithms.

Ocean polarimetry requires off-glint measurements with high polarimetric accuracy and high spatial resolution to detect small-scale variations of the polarized light in the ocean [30]. Off-glint measurements (near-principle plane measurements $\sim 30^\circ$ to 60° azimuth angle) are more useful for ocean polarimetry to reduce the glint-contaminated pixels while still having a sufficient upwelling polarized signal. Simultaneously, the principal plane measurements are essential for aerosol and cloud polarimetry to maximize the

range of scattering angles. The high polarimetric accuracy of the APS/RSP ($<0.2\%$) and SPEXone/SPEX (0.3 - 0.5%) instruments makes them well suited for the ocean polarimetry applications; however, their polarimetric coverage for the oceanic scenes are limited due to their along-track scanning design. AirMSPI, the MAIA prototype instrument, can collect multi-angle observations of the scene between $\pm 67^\circ$ using a motorized gimbal system, despite that AirMSPI is designed to target land-based populations with the objective of monitoring and evaluating the public health with polarimetric accuracy $<1\%$. SPEXone and HARP2 onboard the upcoming PACE mission will collect multi-angle polarized observations over Earth's atmosphere, land surface, and ocean. SPEXone is specifically designed to enable measurements of optical and micro-physical properties of aerosols with unprecedented detail and accuracy. HARP2 is primarily designed to measure aerosol particles and clouds, as well as properties of land and water surfaces. Although SPEXone and HARP2 are principally designed for the remote sensing of aerosol and cloud, respectively, the combined polarimetric datasets from both instruments are expected to provide insights for the ocean polarimetry, yet with a limited spatial resolution (3-5 km).

VICO, the presented instrument, is designed to collect hyper-angular linear polarization at four visible and NIR spectral channels in an imaging mode, as done with the HARP2/PACE instrument, but with higher polarimetric accuracy, similar to the SPEXone/PACE instrument. The accuracy level in the measured VICO DoLP is better than 0.25% [25] with small sufficient angular resolution ($\sim 0.12^\circ$). In addition, VICO is a pointing instrument (gimbaled system), which makes it suitable for ocean color applications by allowing the measurement of the polarized light field in and off the principle-viewing plane. VICO design and specification make it a retrieval-capable instrument providing a better characterization of the aerosol and hydrosol properties. The polarimetric dataset acquired by the instrument is expected to be utilized to verify data processing and validate algorithm performance for spaceborne polarimeters such as HARP2 and SPEXone on the forthcoming PACE observatory. The instrument is discussed in more detail in the following section and in Bowles (2015) [25].

3. Data and uncertainties

In this section, we provide an overview of the field campaigns and the instruments used in this work. An assessment of uncertainty propagation for the collected data parameters is also discussed in the following subsections.

3.1. Data

Measurements from two case studies, representative of both coastal and open ocean regimes, were analyzed in this article. The first case, noted Case 1, was made on September 8, 2012, near the open ocean region of south Florida ($24^\circ 32.504' \text{ N}$, $-81^\circ 2.516' \text{ W}$). Coastal measurements were made on August 29, 2014, in the Chesapeake Bay coast ($38^\circ 57.917' \text{ N}$, $-76^\circ 23.767' \text{ W}$) (noted Case 2). Maps of the geographical locations for each case are shown in Fig. 1. The figure shows a true-color image overlaid with chlorophyll-a concentration (Chl-a) retrieved from MODIS-Aqua on August 31, 2014. Chl-a in Fig. 1 represent values that are typically found in each case.

3.1.1. Airborne measurements

The main remote sensing instrument used for both case studies is the aircraft-based Versatile Imager for the Coastal Ocean (VICO) developed by the Naval Research Laboratory (NRL). The design, fabrication, calibration, and airborne deployment methodologies of VICO (Table 1 and Fig. 2.) are described in more detail by Bowles

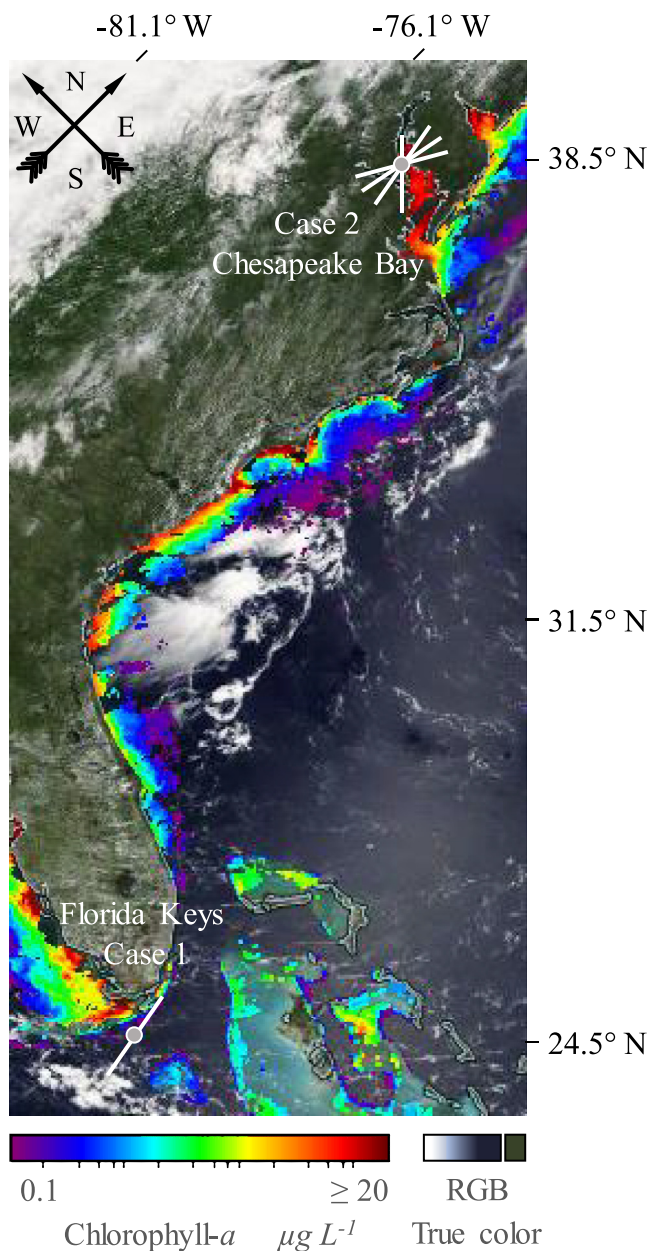


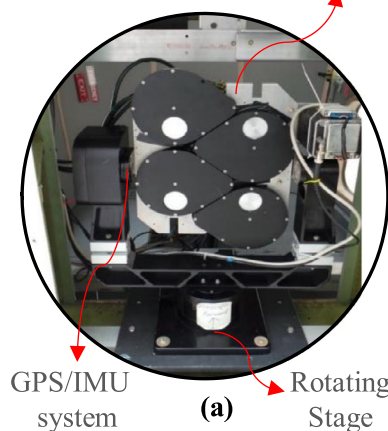
Fig. 1. Maps showing the geographical locations of in situ sites corresponding to open ocean waters (noted Case 1) and coastal waters (noted Case 2) types. The aircraft flight line patterns used in this study are also shown. The figure shows a true color image as it was observed by MODIS-Aqua on August 31, 2014. The image is overlaid by the retrieved Chlorophyll-a concentrations.

Table 1

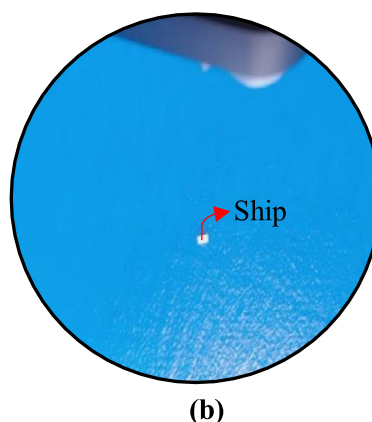
VICO Instrument Specifications. CCD, and FOV stand for Charge-Coupled Device and full angle Field-Of-View, respectively. The passband bandwidth of each of the spectral channels is shown in parentheses.

Property	Value
Focal Plane Technology	12-bit interline transfer CCD
Focal Plane Size	4872 × 3248 pixels
Spectral Channels	435 (20), 550 (10), 625 (10), 754 (10) nm
FOV	40° × 26°
Max Frame Rate	3 Hz
Nominal Frame Rate	1 Hz

Four cameras with tear drop-shaped filter wheels mounted on a plate



GPS/IMU system (a) Rotating Stage



(b)

Fig. 2. (a) The NRL VICO instrument. (b) VICO true color image over the area of interest.

et al. [25]. To briefly summarize, VICO provides multi-spectral radiance and linear polarization images at high spatial resolution with a ground sample distance (GSD) of 22 cm at nadir from a height of 1525 m. Measurement of linear-polarization was obtained using a four-camera system. The cameras are rigidly mounted on an aluminum plate automatically controlled by a rotating stage to allow imaging at different viewing angles. A wire grid polarizer is placed over each camera with orientations at 0°, 45°, 90° and 135° relative to the vertical. The 0° filter is aligned with the forward-to-aft axis of the aircraft. A motorized filter wheel is attached in front of each polarizing filter to provide multi-spectral measurements from the system. The filter wheel contains five-positions; four contain narrow-band spectral filters centered at 435, 550, 625, and 750 nm and the last position was used for the dark current measurements. A combined global positioning system (GPS) with an Inertial Measurement Unit (IMU) was mounted on the rotating stage to record the attitude and position information. The position was also supplied by a more accurate second GPS/IMU system, C-miniature integrated GPS/INS tactical system (C-MIGITS), installed on the airframe. The attitude and position information from the rotating stage and airframe were both used in the geometric processing to determine the geographical positions and viewing angles of each pixel in the data. The cameras imaged at a rate of about 1.1 Hz, limited by the speed of the filter wheels, to provide radiances measured with the linear polarizers oriented in the 0°, 45°, 90°, and 135° directions. The radiance values recorded from the four cameras are denoted by I_0 , I_{45} , I_{90} , and I_{135} . The calibrated value of each recorded radiance was then used to compute the linear Stokes

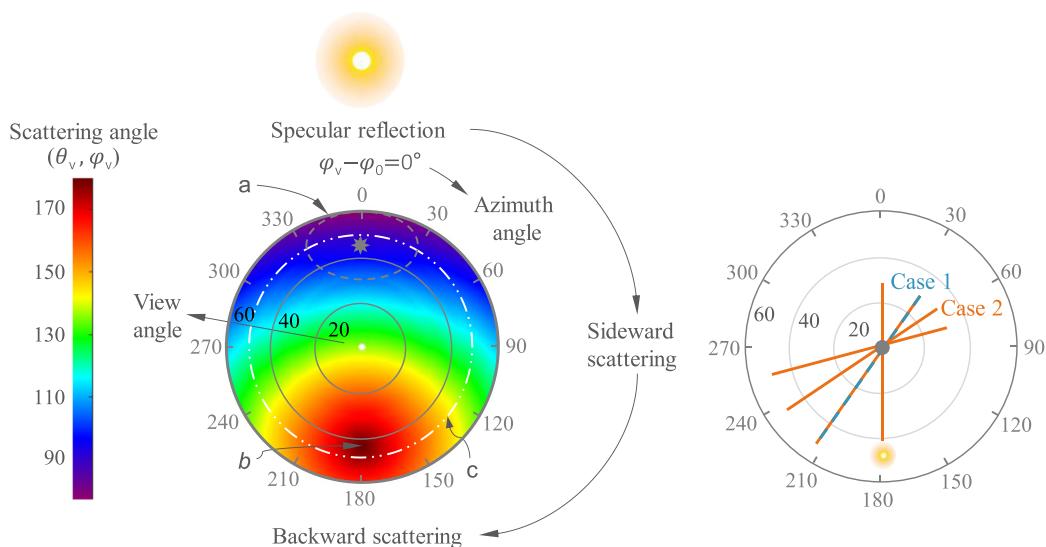


Fig. 3. The left-hand panel shows polar plot of the viewing angles and the specular and backscattering planes in observations and simulations of the upwelling light field. The viewing angles are plotted as a function of scattering angles in units of degrees. The right-hand panel shows a polar plot of each VICO flight line for Case 1 and Case 2 sites. The solar zenith and azimuth angles are at $\theta_0 = 44^\circ$, and $\phi_0 = 110^\circ$, respectively for both cases. The anti-solar point (backscattering direction) indicated by a yellow sun disk at $\theta_0 = 44^\circ$. Note that, the aircraft azimuth is relative to the Sun's azimuth ($\phi_v - \phi_0 = 0$). The letters a, and b in the left-hand polar plot indicate the sunlight region, and the anti-solar point for $\theta_0 = 44^\circ$, respectively. The white dash circle, indicated by the letter c, projects the underwater Snell window boundary on the viewing geometry ($\theta_v = 48^\circ$ for the underwater viewing perspective).

parameters of the incoming light observed at the aircraft altitude as follows (Eq. (1)):

$$\bar{S}^{obs} = \begin{bmatrix} I \\ Q \\ U \end{bmatrix} = \begin{bmatrix} 0.5(I_0 + I_{90} + I_{45} + I_{135}) \\ I_0 - I_{90} \\ I_{45} - I_{135} \end{bmatrix} \quad (1)$$

where I is equal to the total radiance. Q and U together specify the state of linear polarization to the local meridional plane of reference. All parameters are spectrally and geometrically dependent ($\theta_v, \phi_v, \lambda$).

The polar angles diagram in Fig. 3 shows the viewing angles and where the specular and backscattering planes are in the observations and simulations. The figure shows a polar plot of scattering angles as a function of viewing zenith and viewing azimuth angles in units of degrees. The viewing zenith angle (θ_v) is shown as the radial distance of the polar diagram. The radial distance ranges from 0° at the origin point to 60° at the circumference. The viewing azimuth angle (ϕ_v) is shown as the polar angles of the diagram measuring 0° at the top moving clockwise in a 360° circle. The position of the Sun is at $\theta_0 = 44^\circ$ and $\phi_0 = 110^\circ$ for both of the VICO observation cases. The viewing azimuth angles ϕ_v are adjusted relative to the Sun's azimuth defining the solar scattering geometry in the principal plane. The diagram can be interpreted by considering an observer standing at the center of the polar plot. The viewer looks in the Sun's azimuth direction when $\phi_v = 0^\circ$. A Sun disk is shown on the top of the diagram indicating the solar principal plane direction, the specular direction at $\phi_v = 0^\circ$ (top) and the backscattering direction at $\phi_v = 180^\circ$ (bottom). The specular reflection from the water surface, the direct transmission through the atmosphere from the Sun to the surface and from the surface to the detector, is indicated by a white star at $\phi_v = 0^\circ$ and $\theta_v = 44^\circ$. The white dash circle shows the border of the Snell window ($\theta_v = 48^\circ$).

The aircraft data are taken in what is called a star pattern. The rotation stage attempts to keep the VICO instrument pointed at the same location on the ocean surface, called the image center. The aircraft then makes multiple passes over that point, with each

pass occurring with a different aircraft azimuthal direction relative to the Sun. During each of these runs, the VICO is taking data. The local zenith angle changes at a rate that scales with altitude and aircraft speed and also changes based on the proximity to the image center. That rate is slower when farther away and reaches a maximum rate as the plane overflies the image center. During the imaging, various frames are taken for each color that overlap in the zenith/azimuth space. The right-hand panel of Fig. 3 shows a polar plot of VICO multiple passes and the solar zenith direction for both cases.

3.1.2. Shipborne measurements

Water optical properties were measured using Sea-Bird Scientific/WET Labs instruments carried out by NRL research vessels. Absorption and attenuation in the seawater were measured at different depths by the spectral absorption-attenuation spectrophotometers (ac-s) and the ac-9 meter. The ac-s meter was used to measure the particulate absorption and attenuation at 83 wavelengths in the 400-750 spectral range. The ac-9 meter was used to measure the colored dissolved organic matter absorption at nine wavelengths in the 412-715 nm spectral range. The backscattering was measured at three angles (100° , 125° , and 150°) and three wavelengths (450 nm, 530 nm, and 650 nm) using the three-angles, three-wavelengths Volume Scattering Function meter ECO-VSF3. Salinity, temperature, and depth were measured by the integrated Conductivity Temperature Depth (CTD) sensor (SBE 49). Temperature and salinity were used with the pure water to correct the absorption and attenuation measurements from the ac-s and ac-9 instruments. All instruments were calibrated before and after each deployment. The left column of Fig. 4 shows the corresponding in-water optical properties measured in each case.

Fluorometric measurements of Chlorophyll-a fluorescence were also available from a calibrated WETStar fluorimeter. Although it is widely accepted to relate chlorophyll-a concentration to the chlorophyll-a fluorimeter measurements, the relationship suffers from some limitations due to the influence of incident irradiance. Variations in incident irradiance influence the chlorophyll-a fluorescence non-photochemical quenching, thus leads to variable es-

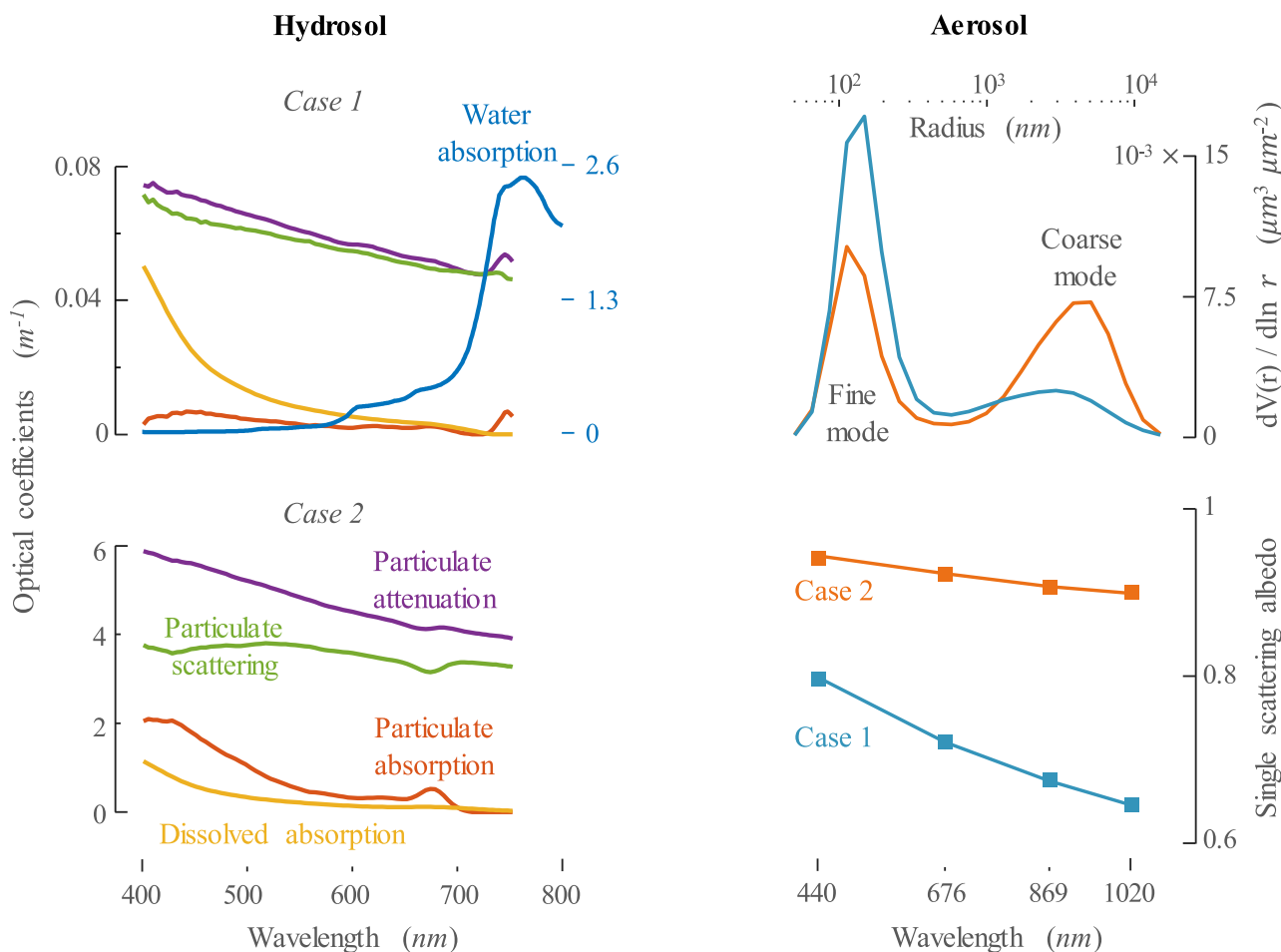


Fig. 4. The optical properties of hydrosol (left column) and aerosol (right column) for Cases 1 and 2 sites. The left column shows the spectra absorbed (orange), scattered (green), and attenuated (purple) by the seawater particles. The spectra absorbed by the Coloured Dissolved Organic Matter (CDOM) and water molecules are shown in yellow and blue, respectively, in the left column. The right column shows the spectral Single Scattering Albedo (SSA) and the aerosol size distributions as a function of radius. The aerosol and ocean optical coefficients are derived from the remote sensing aerosol network (AERONET) and the ac-s meter measurements, respectively.

timates of chlorophyll-a concentration [82]. Because of this potential limitation, we estimated the Chl-a from measured absorption spectra from the ac-s meter. Chlorophyll concentration was determined from a baseline value of the particulate absorption peak in the red waveband [82]. The method was shown to be primarily related to chlorophyll-a concentrations extracted by the high-performance liquid chromatography (HPLC) over a variety of phytoplankton cultures and different water types, thus making it a more effective method to use for the chlorophyll-a concentration estimation. The peak is computed from the line-height absorption at 676 nm above a linear background between 650 nm and 715 nm. The baseline background is used to remove the contributions from non-algal particles and the minor contributions by accessory pigments. The phytoplankton absorption peak is primarily associated with chlorophyll-a in the red waveband due to much lower pigment packaging compared to the absorption peak in the blue waveband.

Concentrations of mineral particles were also estimated from the measured absorption, and attenuation spectra based on the strong relationship observed between in situ measurements of the scattering coefficient at 555 nm, and the concentration of total suspended solids (TSS), particulate organic matters (POC), and particulate inorganic matters (PIC) [83,84]. The particulate scattering coefficient was obtained from the difference between the particulate attenuation and absorption coefficients.

Ship-based aerosol optical depth (AOT) measurements were made using the Microtops II sunphotometer (Solar Light Co., Inc). Microtops estimates spectral AOT from the measured direct solar irradiance at five wavelengths, namely 340 nm, 440 nm, 675 nm, 870 nm, and 936 nm.

3.1.3. Other measurements

Measurements from the closest available ground-based Aerosol Robotic Network, (AERONET) were used to obtain more detailed aerosol parameters for each measured site [85]. AERONET provides estimates of the spectral Aerosol Optical Thickness (AOT), effective radius (r_{eff}), volume median radius (V_{eff}), standard deviation (σ), and volume concentrations (C_v) for both fine and coarse modes of the aerosol size distributions [86]. The parameters are derived from the direct and diffuse spectral sun radiation of the total atmospheric column measured by the multiband CE-318 sun photometer (CIMEL Electronique). We used the data from Key Biscayne and GSFC AERONET sites located approximately 80 and 20 nautical miles away from Cases 1 and 2 sites, respectively. A summary of the aerosol and hydrosol parameters used is shown in the right column of Fig. 4 and Table 2.

3.2. Uncertainty

The uncertainties of the measured radiances and their consequently derived products can be estimated using various methods

Table 2

Aerosol and hydrosol parameters used for Case 1 and Case 2 sites. The wind speed is 3 m/s for both cases. Fine/Coarse is the aerosol mode fraction. m_{fine} and m_{coarse} are the complex refractive indices of the fine and coarse aerosol particles, respectively. Chla, POM, and PIC are the concentrations of Chlorophyll-*a*, Particulate Organic Matter, and Particulate Inorganic Matter, respectively. c_p and b_p are the particulate attenuation and scattering coefficients, respectively. a_p and a_g are the particulate and dissolved absorption coefficients, respectively. AOT, SSA, and the IOPs are all given at the 440 nm band.

	Parameter	Units	Case 1 (Open Ocean)	Case 2 (Coastal)
Aerosol	Fine/Coarse	%	43	69
	m_{fine}	unitless	1.40 + $i0.02$	1.47 + $i0.007$
	m_{coarse}	unitless	1.45 + $i0.07$	1.53 + $i0.001$
	AOT	unitless	0.094	0.057
	SSA	unitless	0.65	0.094
Hydrosol	Chla	$\mu\text{g L}^{-1}$	0.01	20
	POM	$\mu\text{g L}^{-1}$	0.25×10^3	5.8×10^3
	PIM	$\mu\text{g L}^{-1}$	0.08×10^3	16×10^3
	c_p	m^{-1}	0.0715	5.62
	b_p	m^{-1}	0.0650	3.67
	a_p	m^{-1}	0.0065	1.95
	a_g	m^{-1}	0.0280	0.67

from the literature [87-90]. Monte Carlo method provides numerical estimates of the uncertainties, where the exact shape of the uncertainty distributions of the underlying variables is considered. The technique is capable of handling the non-linearity and discontinuity in complex derived models. It is deemed to be robust, but the added mathematical complexity can be computationally intensive to implement within the pixel-by-pixel routine data processing of ocean color. In practice, the analytical law of propagation [91] is commonly used to approximate uncertainties in the ocean color products [89,92,93], where propagated errors are obtained from assumed normal uncertainty distributions. A recent comparison was made between Monte Carlo and the law of propagation framework, showing a good agreement in estimating uncertainties for several ocean color products [89]. In this article, we use the analytical law of propagation [87] to propagate uncertainties from the measured polarized radiance to the derived parameters. The square of the total uncertainty of each parameter, u_x^2 can be estimated using the variance-covariance matrix of the polarized radiance inputs, $V_{L,polarized}$ and the Jacobian matrix, \mathbf{J} as:

$$u_x^2 = \mathbf{J} V_{L,polarized} \mathbf{J}^T \tag{2}$$

Where x is the target parameter such as I , Q , and U and u_x^2 is the square of the total uncertainties for each of the target parameter u_I^2 , u_Q^2 , and u_U^2 . The square of the total radiance uncertainty, u_I^2 can thus be estimated from the means and variances of measured polarized radiance quantities as:

$$u_I^2 = \begin{bmatrix} \frac{\partial I}{\partial I_0} & \frac{\partial I}{\partial I_{45}} & \frac{\partial I}{\partial I_{90}} & \frac{\partial I}{\partial I_{135}} \end{bmatrix} \times \begin{bmatrix} \sigma_{I_0}^2 & \sigma_{I_0 I_{45}} & \sigma_{I_0 I_{90}} & \sigma_{I_0 I_{135}} \\ \sigma_{I_{45} I_0} & \sigma_{I_{45}}^2 & \sigma_{I_{45} I_{90}} & \sigma_{I_{45} I_{135}} \\ \sigma_{I_{90} I_0} & \sigma_{I_{90} I_{45}} & \sigma_{I_{90}}^2 & \sigma_{I_{90} I_{135}} \\ \sigma_{I_{135} I_0} & \sigma_{I_{135} I_{45}} & \sigma_{I_{135} I_{90}} & \sigma_{I_{135}}^2 \end{bmatrix} \times \begin{bmatrix} \frac{\partial I}{\partial I_0} \\ \frac{\partial I}{\partial I_{45}} \\ \frac{\partial I}{\partial I_{90}} \\ \frac{\partial I}{\partial I_{135}} \end{bmatrix} \tag{3}$$

where the diagonal elements of $V_{L,polarized}$ are equal to the square of the uncertainties in the measured polarized radiance quantities,

I_0, I_{45}, I_{90} and I_{135} , and the off-diagonal elements are the covariances between them. For the total radiance calculations, we can start by computing the partial derivatives in Eq. (3):

$$\mathbf{J} = \begin{bmatrix} \frac{\partial I}{\partial I_0} & \frac{\partial I}{\partial I_{45}} & \frac{\partial I}{\partial I_{90}} & \frac{\partial I}{\partial I_{135}} \end{bmatrix} = \begin{bmatrix} \frac{1}{2} & \frac{1}{2} & \frac{1}{2} & \frac{1}{2} \end{bmatrix} \tag{4}$$

Therefore, the square of the total radiance uncertainty can be calculated as:

$$u_I^2 = \frac{1}{4} \left(\sigma_{I_0}^2 + \sigma_{I_{45}}^2 + \sigma_{I_{90}}^2 + \sigma_{I_{135}}^2 + 2(\sigma_{I_0 I_{45}} + \sigma_{I_0 I_{90}} + \sigma_{I_0 I_{135}} + \sigma_{I_{45} I_{90}} + \sigma_{I_{45} I_{135}} + \sigma_{I_{90} I_{135}}) \right) \tag{5}$$

The total uncertainties of all parameters are derived from correlated input quantities. The off-diagonal elements of the variance-covariance matrices are considered in the calculations. All the variance-covariance parameters are calculated from VICO measurements. Similarly, we can compute the total uncertainties for each of the target parameters. Partial derivatives and total uncertainties of each target parameter in this study were calculated analytically, and are given in the appendix.

Several random and systematic processes impact the radiometric accuracy. Laboratory work was performed to identify and quantify the sources of uncertainty and error in the system [25]. The typical radiometric uncertainties and errors of the system can add up to 4.5%. The radiance uncertainty and error levels in a single-pixel of the data can be expressed as, $1.1^{0.022} \pm 0.027 \mu\text{W cm}^{-2}\text{sr}^{-1}\text{nm}^{-1}$, where 1.1 is the measured radiance value at the blue band of Case 2 (I_{Blue}), and ± 0.027 is the systematic uncertainties ($\approx 2.5\%$) associated with the output radiance of the integrating sphere (1.5%) plus the process of transferring calibration to the integrating sphere (1%) [94]. The radiance exponent, 0.022, represents the photon statistics errors ($\approx 2\%$) due to stray light, shot noise, dark noise, and filter positions.

Fortunately, errors from the rotational positions of the polarizing filters can be corrected from any misalignment. Although the polarizer's transmission axes were placed as closely to $0^\circ, 45^\circ, 90^\circ$ and 135° angles as possible, the position of the polarization filters η_{1-4} were rechecked after installation and corrected for any misalignment errors during polarizers placement. First, an experiment was conducted using the integrating sphere and a reference polarizer with a precisely known transmission axis. The polarizer was used to calculate the polarizer orientations in the system, within the uncertainty limits of the reference polarimeter. Any offset α_{1-4} in the polarizer's orientations were then determined, and a correction method was used to re-orient the system into the proper reference plane (see chapter 3 Ref. [95]). The correction matrix that re-distribute the energy in the VICO detected Stokes vector is derived as:

$$\mathbf{C} = \begin{bmatrix} 1 & a & b \\ 0 & \cos 2(\eta_1 + \alpha_1) - \cos 2(\eta_3 + \alpha_3) & \sin 2(\eta_3 + \alpha_3) - \sin 2(\eta_1 + \alpha_1) \\ 0 & \cos 2(\eta_2 + \alpha_2) - \cos 2(\eta_4 + \alpha_4) & \sin 2(\eta_4 + \alpha_4) - \sin 2(\eta_2 + \alpha_2) \end{bmatrix}^{-1} \tag{6}$$

where a and b are defined as:

$$a = \cos 2(\eta_1 + \alpha_1) + \cos 2(\eta_2 + \alpha_2) + \cos 2(\eta_3 + \alpha_3) + \cos 2(\eta_4 + \alpha_4)$$

$$b = -\sin 2(\eta_1 + \alpha_1) - \sin 2(\eta_2 + \alpha_2) - \sin 2(\eta_3 + \alpha_3) - \sin 2(\eta_4 + \alpha_4)$$

Additionally, data binning and multiple measurements averaging can significantly reduce the system uncertainties. Two binning or averaging steps are possible for the collected data. First, since the focal planes are high-resolution (4872×3248 pixels), the data can be significantly binned while maintaining the desired angular resolution. Second, the data can be averaged across the overlapped frames that are taken during the multiple flight passes (as described in Sec. 2.1.1 above). A 16×16 pixel binning is used in the data processing. The data were also averaged across overlapping frames (four frames on average) for each viewing direction in the

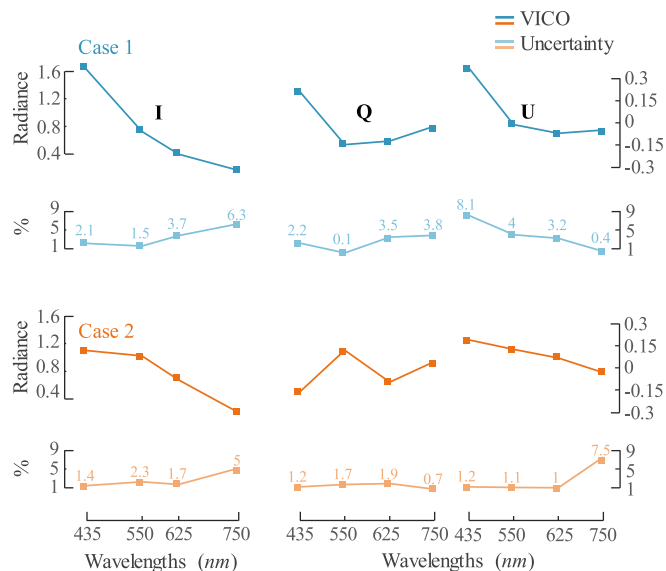


Fig. 5. At-sensor Stokes parameters and the corresponding uncertainty in percent derived from the 16×16 pixels binning for Case 1 and Case 2. Radiances are given in units of $\mu W cm^{-2} nm^{-1} sr^{-1}$. It is important to note that the presented uncertainties in this figure come from the measuring instrument errors and uncertainties combined with several other environmental factors such as capillary ocean waves and shadowing of one facet by another, which add up to the magnitude of the quantified laboratory radiometric uncertainties and errors. The increased uncertainties at the longer wavelength can be primarily attributed to either an atmospheric spatial variation, and sea surface contamination (ex. sunglint, and whitecaps) in the field.

scene. Since the nadir viewing angles were revisited from several flight lines, there were more frames to average for these angles; however, the number of frames to average is limited by the flight speed at these viewing angles. The use of data binning or averaging provides a proper balance between the angular resolution and the dynamic range of the data to observe the ocean features effectively [25]. The data binning or averaging reduces the angular resolution to a sufficient degree ($\sim 0.12^\circ$) while increasing the signal-to-noise ratio (SNR), allowing for the reduction in the effects of random noise and misregistration (in angle space) of the focal planes.

The overall uncertainties experienced in the field are shown in Fig. 5. The figure shows the Stokes parameters and the corresponding uncertainty percentage using the 16×16 pixels binning ($u_x/\mu_x \times 100\%$, where the uncertainty of each parameter u_x , is scaled by its average value μ_x). It is important to note that the presented uncertainties in this figure come from the measuring instrument errors and uncertainties combined with several other environmental factors such as capillary ocean waves and shadowing of one facet by another, which add up to the magnitude of the quantified laboratory radiometric uncertainties and errors. Regardless of the variability of the environmental condition, the binning improved the radiometric uncertainty to 1.4% at the blue band of the coastal case. However, this uncertainty reduction is not always the case, as seen with the longer wavelength uncertainties of this particular case. The total radiance uncertainty at the 750 nm band is about 5%. The increased uncertainties at the longer wavelength can be primarily attributed to either an atmospheric spatial variation, and sea surface contamination (ex. sunglint, and whitecaps) in the field. A relatively small impact of sunglint is expected given the solar zenith and viewing geometries ($\theta_0=44^\circ$, and $\theta_v=0^\circ$, respectively) and the average windspeed ($W = 3m/s$) compared to a rough ocean surface case [81]. Additionally, the signal levels at the longer wavelength are much lower compare to other VICO channels so that the noise level becomes a higher percentage of the signal.

4. Theory and methodology

We start with optical closures between the observed polarized radiances by the airborne polarimeter, and the in-situ measured water and aerosol parameters by the shipborne and the ground-based AERONET near each site. The in-situ measurements were used in the VRT forward modeling to reproduce the observed polarized radiances at the aircraft level for the different cases. The use of the shipborne and AERONET measurements in this study is necessary to reach a VRT closure that relies on real-world conditions and not based on adjustments of many optical parameters. We then compute the linear Stokes contributions of the atmosphere and extract the water-leaving total and polarized radiances based on the closure achieved between the VRT model and the VICO observation at each case. Finally, we perform a sensitivity study for the impact of the different seawater conditions on the aircraft level and the TOA total and polarized reflectances.

4.1. At-sensor polarized radiance and atmospheric correction

The observed linear Stokes parameters, \vec{S}^{obs} (Eq. (1)) acquired from aircraft or spacecraft over the ocean-surface-atmosphere system (AOS) can be first-approximated by the following expressions:

$$\begin{bmatrix} I \\ Q \\ U \end{bmatrix}^{obs} \cong t_g \left(\begin{bmatrix} I \\ Q \\ U \end{bmatrix}_{(\tau_R, \tau_A, \tau_{RA}, W)}^{atm + sfc} + \left(t_u \begin{bmatrix} I \\ Q \\ U \end{bmatrix}_{(\tau_{IOPs})}^w \div 1 - \bar{r}_{atm} \begin{bmatrix} I \\ Q \\ U \end{bmatrix}_{(\tau_{IOPs})}^w \right) \right) \quad (7)$$

Following the notations demonstrated by Fraser and Gao et al. [96,97], the *atm+sfc* is the sunlight scattered from the combined atmosphere and ocean surface; *w* is the sunlight scattered from beneath the ocean surface and leaving it; t_u is the direct and diffuse upwelling transmittance through the atmosphere for the water-leaving light vector; and t_g is the total atmospheric gaseous transmittance on the sun-surface sensor path, which is assumed to be independent in our process. The divided term, at the end of Eq. (7) $(1 - \bar{r}_{atm})\vec{S}^w$, accounts for the effect of atmospheric reflection of upward water-leaving light vector back to the ocean surface, where \bar{r}_{atm} is the reflectance of the atmosphere.

All the linear Stokes parameters in Eq. (7) are spectrally and geometrically dependent ($\theta_v, \phi_v, \theta_s, \phi_s, \lambda$). The θ_v and ϕ_v are the zenith and azimuth viewing angles from an aircraft or a spacecraft to the ocean surface, respectively. The θ_s and ϕ_s are the solar zenith and solar azimuth angles of the direct sunlight, respectively, and λ is the wavelength. The independent parameters in each linear Stokes vector are defined as follows:

- τ_R Rayleigh optical thickness through the atmospheric profile,
- τ_A Aerosol optical thickness through the atmospheric profile,
- τ_{RA} Interaction term between τ_R and τ_A ,
- W Surface wind speed,
- τ_{IOPs} Total optical thickness through the marine profile by cumulating the optical thickness of each component: water molecules, phytoplankton, Mineral-Like particles, yellow substance, and detritus (Inherent Optical Properties of water constituents).

To obtain the water-leaving radiance and its state of polarization, \vec{S}^w , a thorough calculation of radiation and polarization budget for the atmosphere and ocean surface, *atm+sfc* is required. The

$atm+sfc$ radiation and polarization are necessary to accurately remove the effects of the scattering by atmospheric molecules and aerosols, reflections by the air-water interface scattered [98], and the scattering effects of surface foam [99]. These effects can be determined based on the Rayleigh component, τ_R , the aerosol load, τ_a , aerosol type, and the surface wind speed, W , for each of the measured AOS conditions. We use the VRT model to account for these effects. We compute and remove the $atm+sfc$ contributions from the observed linear Stokes parameters using the VRT model. First, we simulate the atmosphere-ocean system in a forward sense to match the observations at the aircraft altitude using the water optical properties and aerosol parameters measured at each site. Then a second set of the simulation was performed to isolate the $atm+sfc$ contribution, assuming the same atmosphere, and ocean surface, but a fully absorbing ocean (no ocean scattering contribution, $\bar{S}^w = 0$). The $atm+sfc$ contribution was removed from the total observed radiance and polarization by subtracting the observed and $atm+sfc$ linear Stokes parameters using the two sets of simulation. The simulation parameters and the VRT model used are described in the following section.

4.2. Vector radiative transfer modeling

The Ocean Successive Orders with Atmosphere - Advanced (OSOAA) vector radiative transfer code was used to model the field measurement. OSOAA allows the computation of the complete radiance field and the polarization state in a coupled ocean-atmosphere system. It calculates the radiative parameters for each component of the environment, assuming a set of plane-parallel homogeneous layers throughout the atmospheric and marine profiles [27]. The code numerically computes the contribution of each scattering order based on the successive orders of scattering method [100,101]. A detailed description of the code is presented in [102].

The OSOAA model was used in a forward sense to compute radiance and polarization for various viewing angles at the aircraft level. Scattering and absorption by molecules were characterized by their optical depths and depolarization ratio. The OSOAA model does not take into account the gaseous absorption. The effects of gaseous absorption were calculated using the temperature-dependent absorption cross-section data [103,104]. The transmittance spectra of gaseous absorption ($t_g(\lambda)$) was calculated independently based on the empirical relationship [105-107]:

$$t_g(\lambda, \theta_0) = \exp\left(-\frac{[\tau_{O_3}(\lambda) + \tau_{O_2}(\lambda) + \tau_{N_2O}(\lambda) + \tau_{H_2O}(\lambda)]}{\cos \theta_0}\right) \quad (8)$$

where O_3 , O_2 , N_2O , and H_2O are the ozone, oxygen, nitrogen dioxide and water vapor optical thicknesses, respectively, for a given solar zenith angle (θ_0).

The radiative properties of aerosol and hydrosol particles were described by the single scattering albedo, optical depth, and single-scattering Mueller matrix. The coupled atmosphere-ocean system used in these computations is described as follows: The modeled atmosphere consists of air molecules (Rayleigh) and aerosol scatterers. Their amounts (related to their optical thicknesses) vary exponentially with altitude with scale heights of 8 km for molecules and 2 km for aerosols. The aerosol volume distribution is modeled using a bimodal lognormal distribution consisting of fine and coarse modes. Both modes parameterized by volumetric radii, r_v , and standard deviations, σ_v , volumetric concentrations, C_v , as well as complex aerosol refractive index spectra, m . The air/sea interface was modeled for a rough sea defined by the wind speed and the correlated sea surface slope variance for an isotropic slope distribution [108]. The modeled ocean body assumes a homogenous mixture of pure seawater, particulate (phytoplankton, and NAP), and dissolved (CDOM) components.

For realistic Mueller matrices, a hybrid model that combines the analytical Fournier-Forand (FF) phase function with Voss and Fry (VF) reduced Mueller matrices was used for the underwater particles [109]. The VF reduced Mueller matrices, without the magnitude information, effectively provide the normalized light scattering polarization matrix based on real measurements of the ocean waters. The FF analytical model can very well reproduce the shapes of oceanic phase functions, especially at very small angles, based on measured IOPs [110,111]. To construct the particulate phase function, we first normalized the VF Mueller matrices by its scattering function (VF M_{11} (Θ) element) at each scattering angle, and then multiplied by FF scattering function (FF M_{11} (Θ) element) [68]. The variations in the FF phase function is based on the real index of refraction of the particles (m_r), and the Junge slope parameter (γ), for an ensemble of particles that have a hyperbolic particle size distribution (PSD). The real part of the bulk refractive index was calculated from the measured particulate backscattering ratio using the inversion model in [68,112]. Although FF uses only the real part of the index of refraction, the addition of the imaginary part of the index of refraction (the amounts of absorption) does not significantly change the shape of the phase functions generated by FF analytical model [110]. The PSD hyperbolic slope was estimated from the measured particulate attenuation spectrum [113]. Lastly, to obtain the total Mueller matrix of the water body, the pure seawater phase function, similar to Rayleigh scattering, is then mixed by the OSOAA with the particulate Mueller matrix to obtain the total Mueller matrix of the water. To account for molecular anisotropy of water molecules, we used the Rayleigh depolarization factor of 0.039 [114,115].

4.3. Observed parameters

In this article, the bi-directional reflectance ρ , the degree of linear polarization, $DoLP$, and the angle of linear polarization, $AoLP$, are the main parameters we use to describe the incoming light fields at the aircraft observational altitude. They are calculated using the linear Stokes parameters defined in Eq. (1) as follows:

$$\begin{bmatrix} \rho \\ DoLP \\ AoLP \end{bmatrix}^Z = \begin{bmatrix} \rho_u + \rho_p \\ \sqrt{Q^2 + U^2}/I \\ 0.5 \times \tan^{-1}(U/Q) \end{bmatrix} \quad (9)$$

where all parameters are spectrally and geometrically dependent, ($\theta_v, \phi_v, \lambda$) and can be calculated at any given level, Z , for each studied case. The bi-directional reflectance, ρ , is a linear combination of the un-polarized ρ_u and a polarized ρ_p components. The bi-directional reflectance components are the total radiance and the linearly polarized radiance, each scaled by the solar reflected radiation.

$$\begin{bmatrix} \rho_u \\ \rho_p \end{bmatrix} = \frac{\pi r_0^2}{\mu_0 F_0} \times \begin{bmatrix} (1 - DoLP) \times I \\ DoLP \times I \end{bmatrix} \quad (10)$$

where the extraterrestrial solar irradiance [116], F_0 , the cosine of solar zenith angle, μ_0 , and the Sun-Earth distance correction factor, r_0^2 , describes the solar radiation at the top of the atmosphere, TOA.

The advantage of using the reflectance and DoLP parameters is to represent the at-sensor's incoming unpolarized and polarized light independently from the solar radiation, and the choice of a reference plane for the Q and U parameters. Along with that, the error level in DoLP and AoLP parameters must be less since these quantities are derived from measured radiance ratios at the same pixel. This error reduction is only valid with proper calibration of the four separate camera system, thus eliminating the gain and transmission errors due to pixels differences in the final image. The

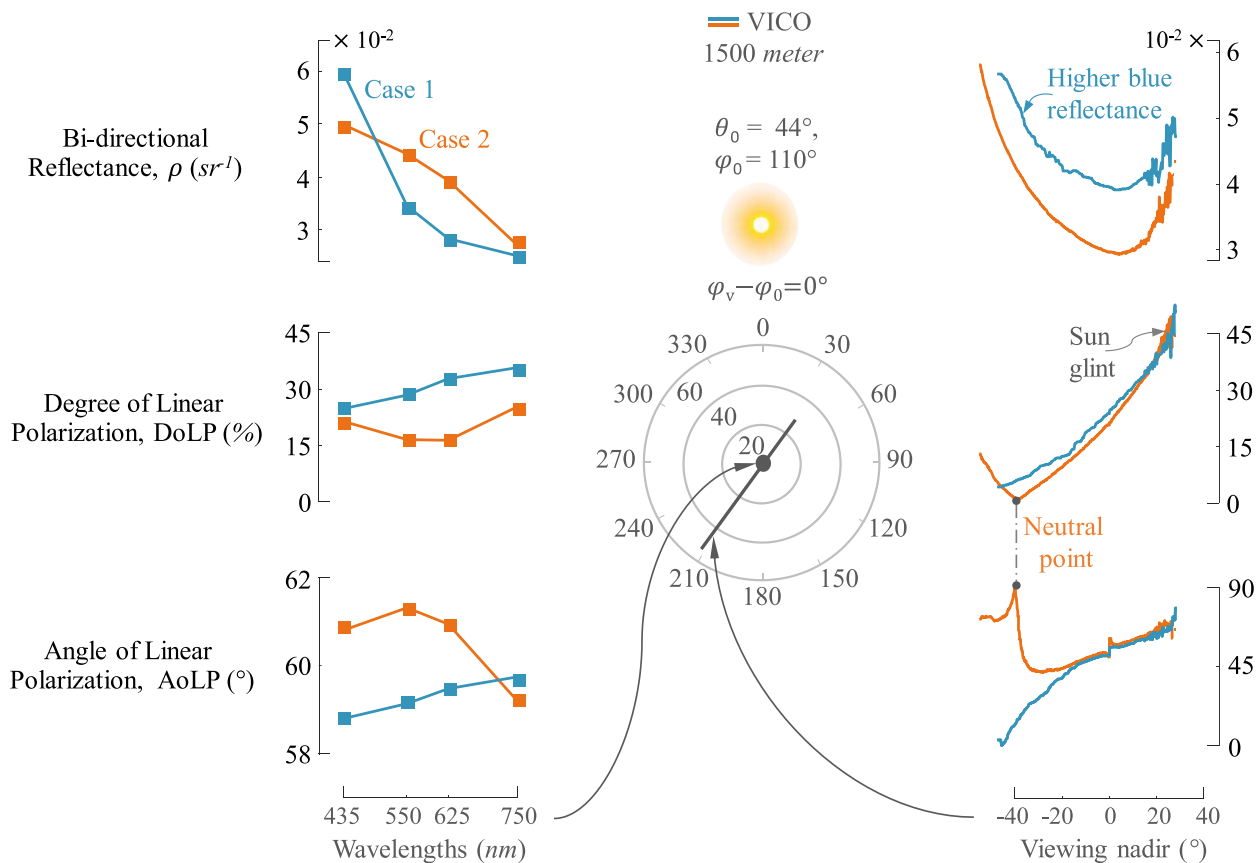


Fig. 6. Relative differences in the spectral and angular total ρ , DoLP and AoLP parameters for the two measured cases. The left-hand panel shows the spectra of each of these parameters at the nadir viewing direction; the right-hand panel shows the 435 nm band of each parameter as a function of viewing nadir angles and at the azimuth line of $\phi_v = 35^\circ$ relative to the Sun. A gray line, in the middle polar diagram of the figure, indicates the flight line pattern of both cases. A Sun disk is shown on the top of the middle polar diagram, indicating the solar principal plane direction, the specular direction at $\phi_v = 0^\circ$ (top), and the backscattering direction at $\phi_v = 180^\circ$ (bottom). The solar position of the Sun was at $\theta_0 = 44^\circ$ and $\phi_0 = 110^\circ$ for both cases. Notice the large AoLP deviation between the two cases coinciding with the DoLP neutral point of Case 2 (gray dot).

systematic errors associated with integrating sphere radiance level also cancels out. Similarly, rescaled linear Stokes parameters (Q/I and U/I) are unaffected by these particular errors. The DoLP accuracy of VICO is better than 0.25% [25].

5. Results and discussion

We describe the results for VICO flying over oligotrophic and turbid water-types. The first water-type, Case 1, is representative of bright blue-like waters found in the large portion of the open ocean and characterized by low Chla concentrations. Scattering and absorption are dominated by phytoplankton and the water molecules themselves. The second water-type, Case 2, is characterized by high Chla, medium non-algal particles, and medium CDOM concentrations representative of green-like waters typically found in productive phytoplankton waters. The atmospheric condition of the first case is characterized by a lower SSA, indicating more absorbing aerosol compared to the second case. The aerosol optical thickness, at 500nm, is about twice lower (0.046) for Case 2 than for Case 1 (0.084). Differences in the measured aerosol and in-water optical properties are shown in Fig. 4 and Table 2 above for both cases. In this section, we first start with the result of VICO [25] observations at different conditions. We then show the results of VRT match to VICO observations and the estimated total and polarized water leaving reflectances. Lastly, we perform an analysis of the total and polarized reflectances variation due to the oceanic parameters used in the VRT modeling of the different conditions. This analysis is described at both the aircraft level and the TOA level.

5.1. Comparison of VICO observations between Cases 1 and 2 sites

In Fig. 6, we highlight the relative differences in the total reflectance, DoLP, and AoLP parameters for the two measured cases. As expected, a higher blue reflectance for the first case across all the nadir viewing geometry partially pertained to the increased scattering in the open ocean case at this band in comparison to the second case. The relative difference between the two cases is high in the green and red bands of the DoLP (10-15%), shown in the spectral DoLP figure (left panel of Fig. 6), and relatively small in overall the AoLP spectra within 3° differences. Another feature observed is that the DoLP crosses a neutral point for Case 2, indicated as a gray dot in the angular DoLP figure (right panel of Fig. 6), whereas that for the first case, the DoLP grazes a neutral point. Notice the corresponding AoLP discontinuity in the second case, marked as a gray dot in the angular AoLP figure (right panel of Fig. 6), and the large AoLP deviation across the nadir viewing direction (0° to 90°) between the two cases.

The differences can be explained by the variation seen in aerosol and ocean optical properties at each observation, shown in Fig. 4 above. The results indicate that small adjustments to the aerosol and ocean microphysical and optical properties can cause unique angular and spectral patterns in the observed total and polarized light field. It is important to note that all the differences are shown at the same viewing angles and illumination conditions for both cases.

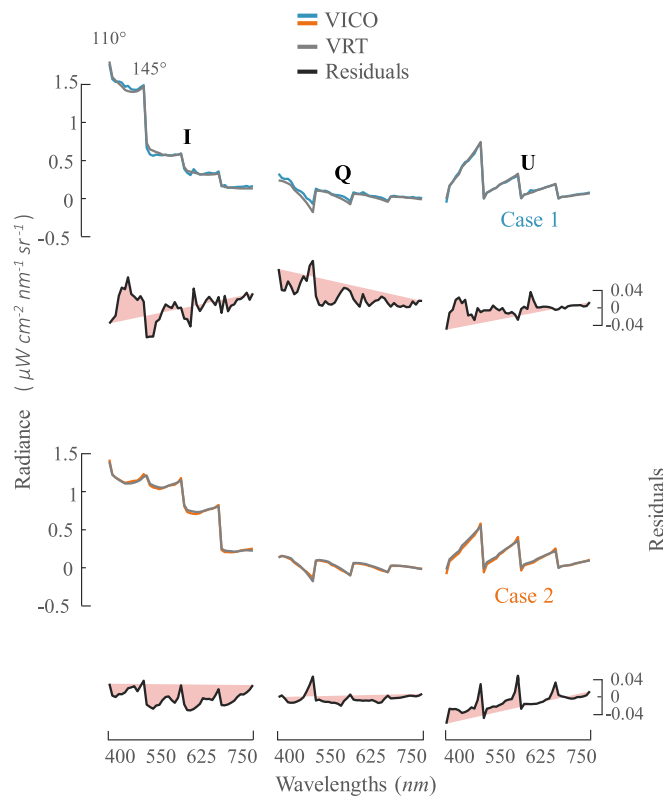


Fig. 7. Multi-spectral, and -angular VRT match with aircraft Stokes parameter (*I*, *Q*, and *U*) observations for Cases 1 and 2. The matches and residuals (i.e., measurement minus model) of the observed parameters are shown in the left and right-hand axes, respectively. The shaded red areas outline the slope of the Stokes parameter residuals across the spectral bands. Each spectral band is shown as a function of scattering angles. The values of the scattering angle 110° and 145° are indicated for each wavelength. The solar position is at $\theta_0 = 44^\circ$ and $\phi_0 = 110^\circ$ for both cases.

5.2. Comparison of VICO measurements with the VRT simulations

In this section, we present the results from the VRT modeling of VICO airborne observations over the two cases. The VRT input parameters were estimated from the atmospheric and oceanic optical properties measured at each location, as described in Section 3.2. The optical properties of both sites are summarized in Table 2 and Fig. 4 above. The multi-spectral and hyper-angular VRT matches are shown in the following subsections.

5.2.1. Multi-spectral and multi-angular VRT match

Figs. 7 and 8 show the spectral VRT match of Case 1 and Case 2 Stokes parameters as a function of scattering angles ranging from 110° to 145°. Case 1, Case 2, and the VRT are color-coded in blue, orange, and gray, respectively. The VRT match is quite consistent with the observed VICO Stokes parameters across the spectrum and the different scattering angles. Slightly less accuracy is noticed in reproducing the *Q* and *U* components, probably due to the AERONET inversion performance. Indeed, adjustments in the AERONET microphysical parameter for the fine aerosol mode tend to further improve the VRT modeling results at the longer wavelengths and viewing angles toward the Sun. As was highlighted previously [117,118], the aerosol retrieval accuracies from AERONET are affected by the lack of using polarization measurements in the AERONET inversion. A higher match accuracy could be possibly achieved by an optimization routine of a complex configurations, however it is important to note that, the VRT models could be also limited. The VRT models are only as good as their internal representation of the physics underlying the modeled atmosphere-ocean system.

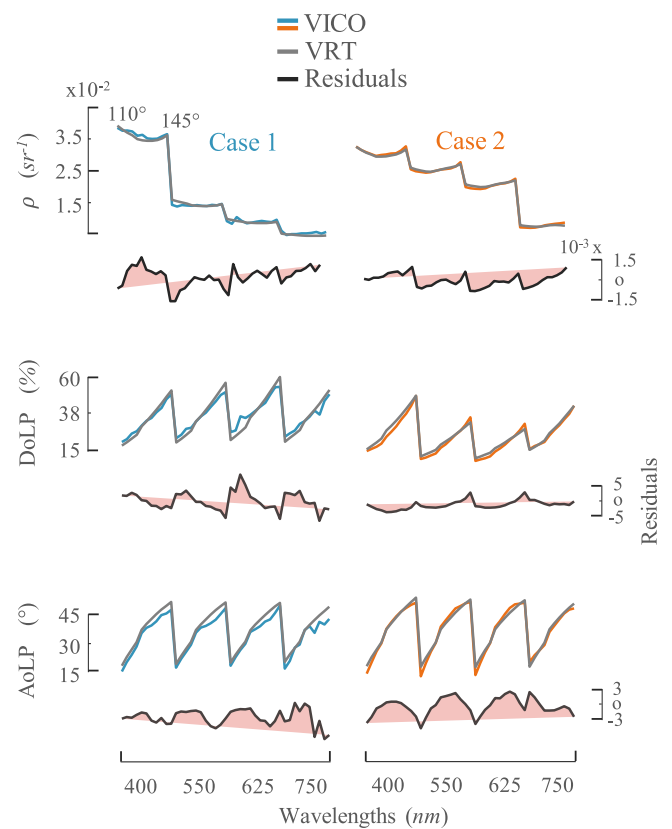


Fig. 8. Multi-spectral, and -angular VRT match with aircraft ρ , *DoLP*, and *AoLP* observations for Cases 1 and 2. The matches and residuals (i.e., measurement minus model) of the observed parameters are shown in the left and right-hand axes, respectively. The shaded red areas outline the slope for each of the observed parameter residuals across the spectral bands. Each spectral band is shown as a function of scattering angles. The values of the scattering angle 110° and 145° are indicated for each wavelength. The solar position is at $\theta_0 = 44^\circ$ and $\phi_0 = 110^\circ$ for both cases.

5.2.2. Hyper-angular VRT match

As described in Sec. 2.1.1, the aircraft was flown in a star-shaped pattern with multiple flight lines to fill the angular space viewed over the area of interest measured by VICO (see Fig. 3). In this flight pattern, all lines crossed a stationary point (the area of interest) where each line defined a different azimuthal space relative to the Sun. The instrument mounting stage was rotated during each flight-line, yielding several sets of images at different viewing angles. The total sampling time of the star-shaped pattern was approximately 15 minutes. The variability of the seawater and atmospheric condition was recorded and analyzed during the flight time using data from the ac-s meter, Microtops, and AERONET. No significant changes were observed. We checked the variability of the AERONET AOD measurements within ± 15 minutes from the aircraft overpass. The AOD values were similar at the different measurement times. The AOD standard deviations were ± 0.002 and ± 0.003 for Cases 1 and 2, respectively.

To visualize the bidirectional changes, we illustrated the results using the polar angles diagram described previously in Fig. 3. In Figs. 9 and 11, we exploit the results of the VRT modeling and VICO observations from many different viewing angles. The radiation and the directionality pattern of the light field are primarily characterized by the illumination condition and by the atmospheric and oceanic optical properties of the observed scenes. The total and polarized light obtained from the coastal water observations at the 443 nm band is described by the Stokes vector components *I*, *Q*, *U*, in Fig. 9, and by the ρ , *DoLP*, and *AoLP* in Fig. 11. The top rows in Figs. 9 and 11 show VICO measurements, and the bottom rows show the corresponding result of the VRT simulations. The

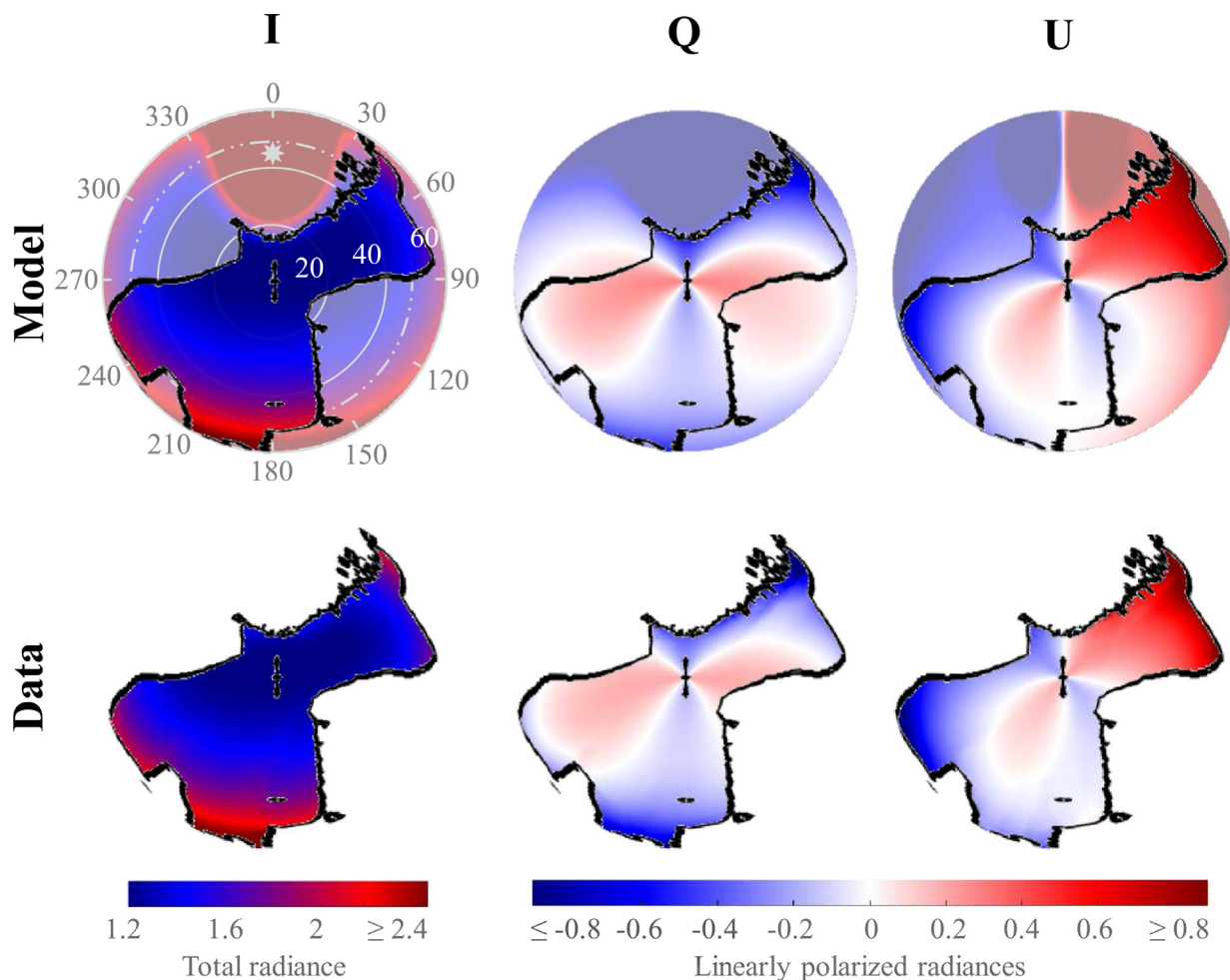


Fig. 9. Hyper-angular VRT match with aircraft Stokes parameter (*I*, *Q*, and *U*) observations. Comparison of the total Stokes components *I*, *Q*, and *U* at different viewing angles. The top row shows the VRT model, and the bottom row shows the VICO measurements. The results are shown for Case 2 and at the 443 nm band. The solar position is at $\theta_0 = 44^\circ$ and $\phi_0 = 110^\circ$. The specular point location is indicated as a white star in the first polar plot in the figure. The white dash circle projects the underwater Snell window boundary on the viewing geometry ($\theta_v = 48^\circ$ for the underwater viewing perspective). Radiances are given in units of $\mu W cm^{-2} nm^{-1} sr^{-1}$.

residuals between measurements and simulations in Figs 9 and 11 are shown in Figs. 10 and 12, respectively. Both figures exhibit considerable match quality. The match is consistent with all the measured viewing angles, thus illustrating that light scattering and absorbing observed features of the atmosphere-ocean systems are well reproduced by the model.

5.2.2.1. Stokes components. The Stokes components match is shown in the unit of radiance in Fig. 9. It is worth noting that the values of *Q* and *U* parameters in Fig. 9 depend on the choice of the plane of reference in the coordinate system described above (meridional plane). Thus, pixel-by-pixel adjustment was considered to geometrically project the *Q* and *U* components on the reference plane of light. For these observations, the *I* component was lowest in nadir direction and largest in the directions toward Sun and near the horizon. The *Q* and *U* components take shape according to Eq. (1). They both switch signs across the viewing geometry, indicating the different planes of polarization observed from the time-averaged radiance measurements and the associated simulations. To define *Q* and *U*, first we pick the (\hat{x} , \hat{y} , \hat{z}) coordinate system as a reference where \hat{x} is the horizontal, \hat{y} is the vertical, and \hat{z} is in the direction of propagation ($\hat{z} = \hat{x} \times \hat{y}$). The Linearly polarized light lying in the *x* or *y* planes can be identified with $U=0$ and $Q>0$ or $Q<0$, respectively. Similarly, for the linearly polarized light lying in the 45° or 135° planes except with $Q=0$ and $U>0$ or $U<0$, respectively. The angular separation from which the magnitude of the

Q pattern decreases to zero occurs roughly at 60° , 150° , 210° and 300° azimuth angles forming an infinity-like shape centered at the origin of the polar diagram (color-coded in white). *U* pattern decreases to zero roughly at 0° , 120° , 180° , and 240° azimuth angles. As expected, the *U* component is precisely zero at the principal plane while the *Q* component is of much higher values ($Q>U$), making the sunglint profile mostly carried by the *Q* component [117,119].

5.2.2.2. Reflectance, DoLP, and AoLP. In Fig. 11, the total reflectance gives similar results as the total radiance in Fig. 9. The DoLP is maximum in the VRT model and the data in and around the specular plane, forming a sunglint profile. Such a feature is uniquely defined by the Sun direct beam and the surface Fresnel reflection parameters at the principal plane of reference. Noticeable changes in the sunglint patterns were observed in the collected images (not shown). Differences in the sea surface roughness affect the symmetry of the sunglint patterns to the principal plane. Sunglint patterns can be a useful tool to yield information about the state of the sea surface, such as the speed and direction of the wind [108] and the flight attitude angles [14]. The radiance and DoLP of sunglint can also be used to cross-calibrate the different wavebands in the visible and NIR wavelengths [74-76] and to retrieve the refractive index of the surface layer [120,121].

The other feature in the data is the formation of neutral points in the DoLP polar diagram. The modeled DoLP shows symmetric

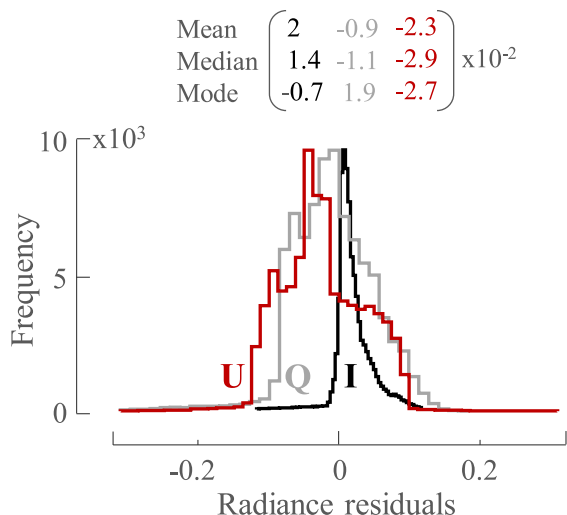


Fig. 10. Stokes parameters residuals (i.e., measurement minus model) for the hyper-angular VRT match shown in Fig. 9. The residuals are shown between VICO measurement and VRT simulation for the I, Q, and U parameters. Radiance residuals are given in units of $\mu W cm^{-2} nm^{-1} sr^{-1}$. The mean, median and mode of the residuals are specified in the figure legend.

neutral points around the principal plane. The measured DoLP confirmed the findings of the neutral point on one of the sides of the

principal plane. Neutral points arise from the zero polarization of the observed light field. This zero polarization can also be seen in Fig. 9 at the viewing geometries where both Q and U neutral lines intersect ($Q=U=0$). The neutral points vary in position with altitude [58] and with different aerosol and hydrosols conditions in the atmosphere-ocean systems [122,123]. Previous studies reported their sensitivity to the imaginary refractive index of absorbing aerosols [20,58], the droplet size distribution in the top layer of clouds [59,124] and the chlorophyll-a concentration in the ocean [14].

Similar results were observed at the different bands of VICO. The angular pattern was generally similar with few differences. The total reflectance decreases as the wavelengths increase primarily due to the decreasing amount of Rayleigh and aerosol scattering from the atmosphere. The DoLP neutral points shift toward the nadir direction with the longer wavelengths [25].

Regardless of how well the models represent the underlying physical process, multiple other factors affect the correctness of both the measurements and the modeling causing the residuals seen in Fig. 12. The observed residuals in this figure could be possibly due to wrong modeling assumptions in the aerosol and hydrosol micro- and macro-physics (ex. refractive indices, particles size, and shapes, etc.), random and systematic photons statistics errors ([25] and Sec. 3.2) caused by the measuring instrument errors and uncertainties in the field, and several other environmen-

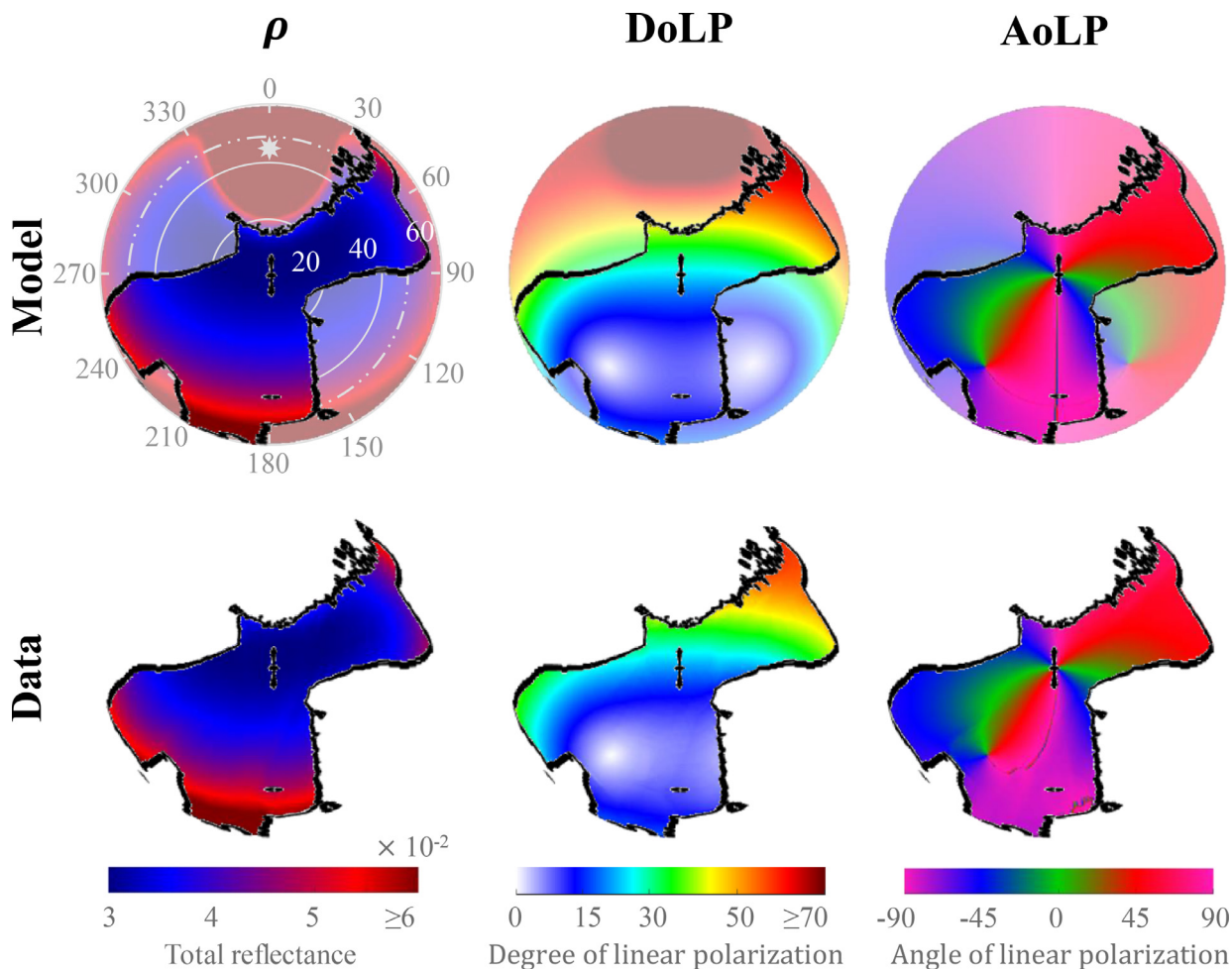


Fig. 11. Hyper-angular VRT match with aircraft ρ , DoLP, and AoLP observations. The top row shows the VRT model, and the bottom row shows the VICO measurements. The results are shown for Case 2 at the 443 nm band. The solar position is at $\theta_0 = 44^\circ$ and $\phi_0 = 110^\circ$. The specular point location is indicated as a white star in the first polar plot in the figure. The white dash circle projects the underwater Snell window boundary on the viewing geometry ($\theta_v = 48^\circ$ for the underwater viewing perspective). The total ρ , DoLP, and AoLP are given in units of sr^{-1} , %, and $^\circ$, respectively.

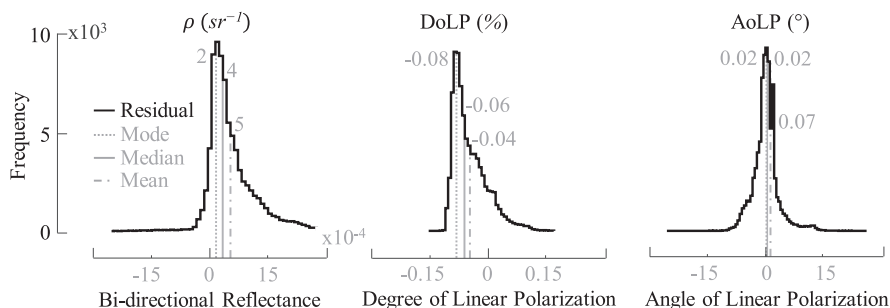


Fig. 12. Residuals (i.e., measurement minus model) for the hyper-angular VRT match shown in Figs. 11. The residuals are shown between VICO measurement and VRT simulation for the total ρ , DoLP, and AoLP parameters.

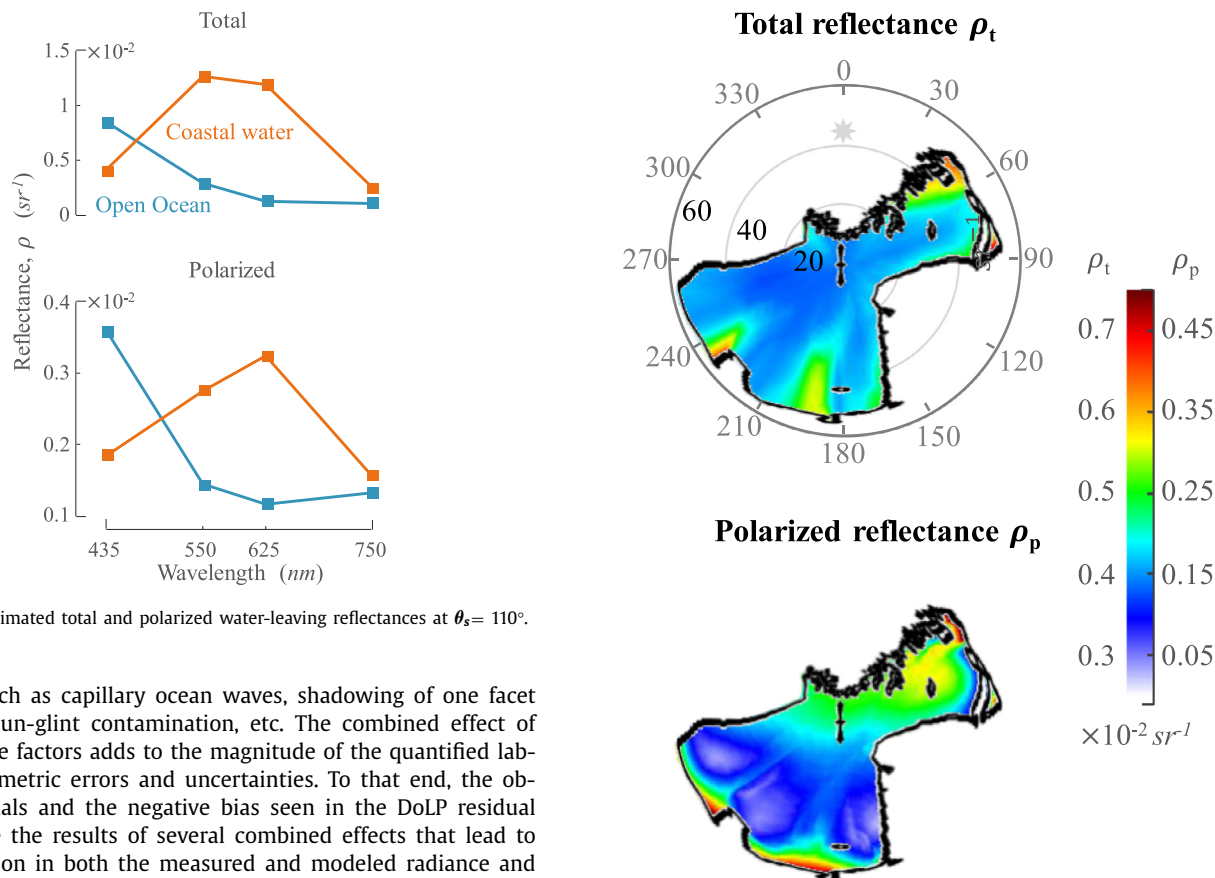


Fig. 13. The estimated total and polarized water-leaving reflectances at $\theta_s = 110^\circ$.

tal factors such as capillary ocean waves, shadowing of one facet by another, sun-glint contamination, etc. The combined effect of these multiple factors adds to the magnitude of the quantified laboratory radiometric errors and uncertainties. To that end, the observed residuals and the negative bias seen in the DoLP residual of Fig. 12 are the results of several combined effects that lead to a misestimation in both the measured and modeled radiance and linear polarization. It is important to note that, regardless of the observed residuals in this figure, the polarimetric accuracy is well within the stated VICO DoLP accuracy ($<0.25\%$), which is not always necessarily the case, given the modeling assumptions made on the unknown variables and parameters and the difficulties experienced in the field measurements.

5.3. Total and polarized ocean reflectance using VICO and VRT

Total and linear polarized water-leaving reflectances were estimated using the VRT computations. The VRT was used to compute and remove the atmospheric path Stokes components using simulations set to run with the atmospheric parameters measured at the time of the imagery acquisitions and with the black ocean body assumption. The retrieved total and polarized water-leaving reflectances are shown in Figs. 13 and 14. In Fig. 13 we show the retrieved water-leaving spectra of Cases 1 and 2. The retrieved spectra are similar to the water-leaving spectra typically found in the open ocean and coastal waters areas. The total reflectance of the open ocean case exhibited higher values at 435 nm, indicat-

Fig. 14. The estimated total and polarized water-leaving bi-directional reflectances of Case 2 at the 443 nm band as a function of viewing angles.

ing more blue water and nearly zero value in the NIR. The coastal water case shows slightly higher values at the NIR band, indicating the presence of higher particulate scattering, such as minerals. In Fig. 14, we show the coastal water observations at the 443 nm band from many different viewing angles. The retrieved polarized reflectances in Fig. 14 are similar to those measured by underwater polarimeters in turbid waters [24,125,126]. The polarized light maximum is approximately at around 100° scattering angle. The polarized light minimum is well off of the principal plane, roughly at $\theta_v = 40^\circ$ to 55° and $\phi_0 = 260^\circ$ to 220° , indicating possible sources of areas of zero, or low, polarization [125]. The impact of the retrieved water-leaving radiance and polarization on the observed total and polarized reflectances at the aircraft and TOA altitudes will be discussed in the following section.

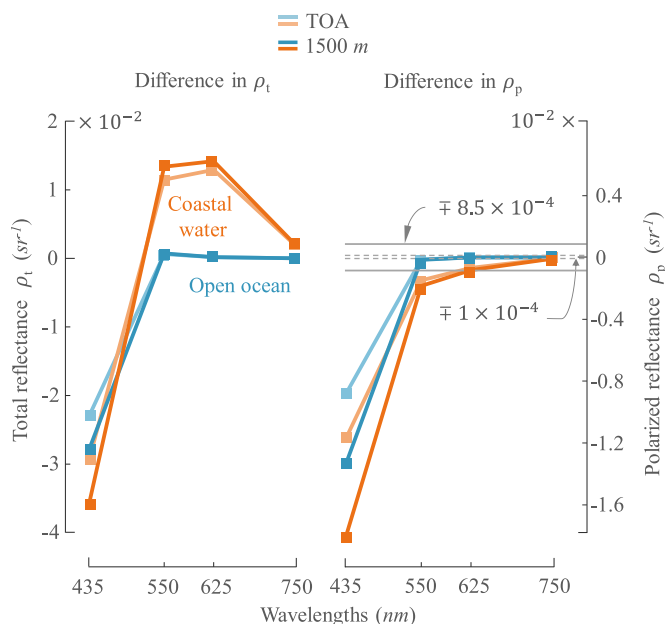


Fig. 15. The spectral differences in total and polarized reflectances obtained from the comparison between the in-water optical properties measured in the open ocean (blue) and coastal water (orange) cases and a pure ocean case (i.e., only molecular scattering and absorption). The differences are shown at $\theta_v = 70^\circ$ and $\phi_v = 35^\circ$, the light blue and light orange curves show the differences at the TOA, and the dark blue and dark orange curves show the differences at the flight altitude (1500 m).

5.4. Sensitivity study for space (or airborne) observations

The aerosol composition primarily determines the top of the atmosphere (TOA) polarized reflectance (ρ_p). Meanwhile, several studies [14,70,117,127] have shown the potential sensitivity of TOA ρ_p to changes in the water optical properties. In this section, the sensitivity of the remotely sensed total and polarized reflectance to the measured in-water optical properties was analyzed at the aircraft altitude and the TOA level. Figs. 15 and 16 show total and polarized reflectance's difference at 1500 m and at TOA when a pure ocean is considered (only molecular scattering and absorption) instead of the one characterized by the measured IOPs. Fig. 15 shows the difference in the spectrum for the open ocean and coastal water cases. The polarimetric accuracy limits of the POLDER instrument ($|\rho_p| > 8.5 \times 10^{-4} \text{ sr}^{-1}$) and of currently achievable accuracies ($|\rho_p| > 1 \times 10^{-4} \text{ sr}^{-1}$) are outlined as solid and dash lines, respectively. It is interesting to note that the total reflectance of the open ocean case and the polarized reflectance of both open ocean and coastal waters are fairly insensitive to the hydrosols at wavelengths greater than 550 nm for the geometrical configuration considered in Fig. 15 ($\theta_v = 70^\circ$, and $\phi_v = 35^\circ$). These wavelengths could thus be preferentially used for the characterization of the atmospheric optical properties. However, such a feature is not true at shorter wavelengths because of the more significant influence of the scattering processes in the water body, as corroborated by the significant differences observed in the total reflectance for the Case 2 water type. For such a latter water type, the polarized reflectance could also be used at short bands with relevance for the detection and characterization of the hydrosols.

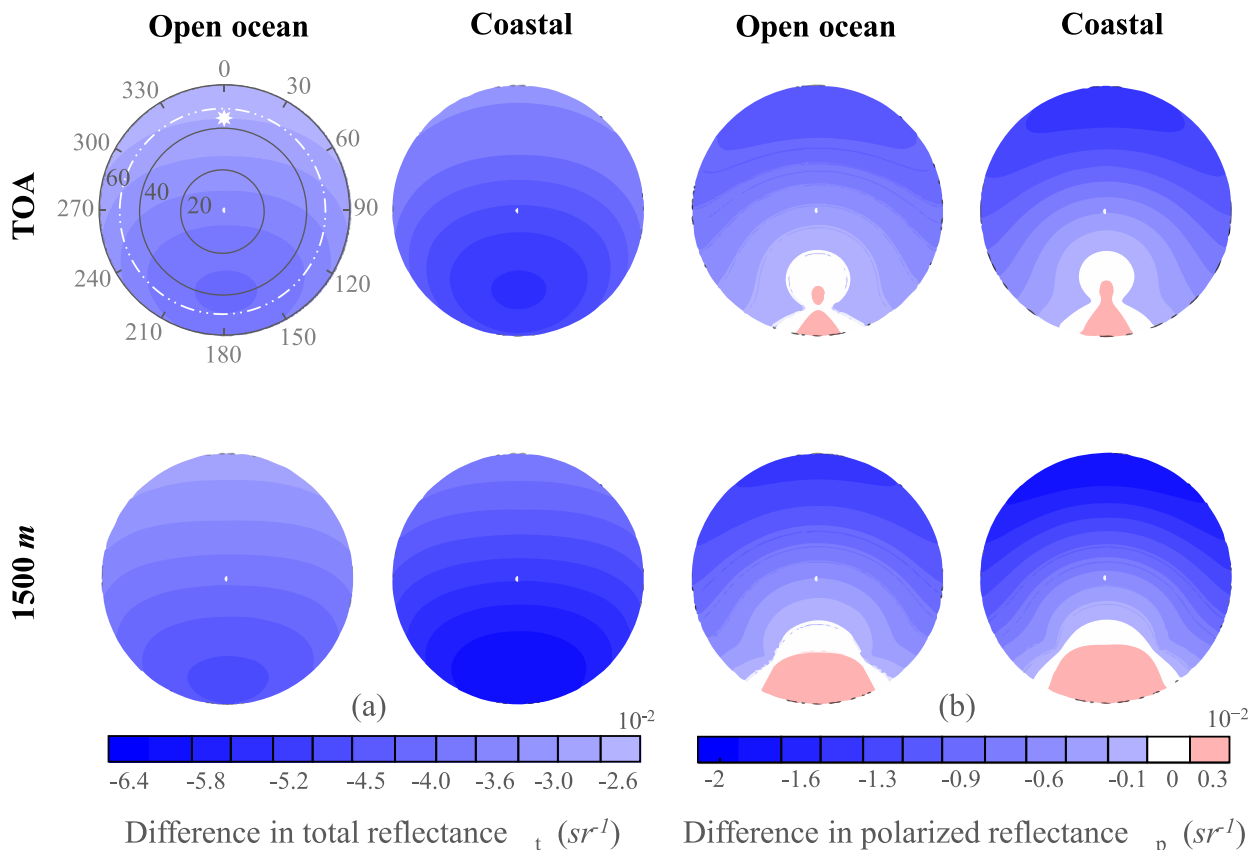


Fig. 16. The viewing angular differences in total and polarized reflectances obtained from the comparison between the in-water optical properties measured in the open ocean and coastal water cases and a pure ocean case (i.e., only molecular scattering and absorption). The differences are shown for the 443 nm band; the top row shows the differences at the TOA and the bottom row shows the differences at the flight altitude (1500 m). The solar position is at $\theta_0 = 44^\circ$ and $\phi_0 = 110^\circ$ for both cases. The specular point location is indicated as a white star in the first polar plot in the figure. The white dash circle projects the underwater Snell window boundary on the viewing geometry ($\theta_v = 48^\circ$ for the underwater viewing perspective). Reflectance values below the polarimetric accuracy limits of POLDER instrument ($8.5 \times 10^{-4} \text{ sr}^{-1}$) are color-coded in white.

Fig. 16 shows the difference across the viewing angles at the 443 nm band for the open ocean and coastal water cases. Reflectance values below the polarimetric accuracy limits of POLDER instrument (8.5×10^{-4}) are color-coded in white. At such wavelength, the polarized reflectance (ρ_p) could be significantly sensitive to the hydrosols across most viewing angles. Again, this is because of the higher amount of the scattering processes induced by the suspended particulate matter, especially in coastal waters. Note that the white areas observed for the polarized reflectance polar plots (Fig. 16b) could be potentially used as relevant geometries to derive information on the aerosols' optical properties from a multi-angular polarimetric satellite or airborne sensor. Therefore, multi-angular polarized reflectance measured from space could be exploited to distinguish the hydrosols from the aerosols from a single observation of a given scene. Note that the sensitivity analysis in Fig. 15 is shown from VICO altitude (1.5 km) and PACE-like observations (TOA). Both altitudes showed polarized reflectance (ρ_p) variation for the open ocean case ranged from -15.4 to $2.6 \times 10^{-3} \text{ Sr}^{-1}$, and -12 to $1.5 \times 10^{-3} \text{ Sr}^{-1}$, respectively. For the coastal water case, the polarized reflectance (ρ_p) ranged from -20.4 to $2.8 \times 10^{-3} \text{ Sr}^{-1}$ and -15.6 to $1.7 \times 10^{-3} \text{ Sr}^{-1}$, respectively. The analysis was also computed for the high altitude NASA ER-2 aircraft (typically 20 km). NASA ER-2 aircraft is frequently used for airborne field experiments and was recently used to deploy several multi-angle polarimeter prototypes during the Polarimeter Definition Experiment (PODEX) [88]. Both NASA ER-2 and TOA altitudes vary in a similar angular pattern with slightly lower magnitude ranges. The NASA ER-2 altitude showed polarized reflectance (ρ_p) variation ranged from -12.3 to $1.6 \times 10^{-3} \text{ Sr}^{-1}$, and -15.9 to $1.8 \times 10^{-3} \text{ Sr}^{-1}$, for the open ocean and coastal cases, respectively (not shown).

6. Summary and conclusion

In this work, we demonstrated the strong consistency between an airborne multi-spectral hyper-angular polarimetric imager and VRT simulations over coastal and clear water conditions. Radiance and linear polarization data were collected in the visible and near-infrared part of the spectrum and at many different viewing angles using the VICO instrument. The observed data have gone through rigorous calibration procedures. Geometric correction is considered for the projection of reference planes of light. The data were adjusted pixel-by-pixel according to their radiometric, spectral, and spatial calibrations. A method has been implemented to propagate uncertainties in the measured polarized radiances and their consequently derived products. The approach is an analytical approximation based on the law of propagation of uncertainty [87,91].

Radiative transfer simulations for the coupled atmosphere-ocean system were run to adequately analyze the observed VICO data with theory. First, the optical properties of aerosol and ocean constituents were measured at different conditions. The measured optical properties were used in forward-modeling to propagate total and linearly polarized radiances to the aircraft altitude. We have shown that the radiance and the linearly polarized light of the observed scenes matches well the VRT simulations. Slightly superior VRT modeling results are achieved with further refinement in the microphysical parameters of the fine aerosol mode. The match was consistent at different wavelengths and at various viewing angles, thus illustrating that light scattering and absorbing features of the atmosphere-ocean systems are well reproduced by simulations.

Second, total and linear polarized water-leaving reflectances were estimated using the VRT computations and the atmospheric parameters measured at the time of the imagery acquisitions. The

reflectance retrievals were similar to those reflectances typically found in coastal and open ocean waters. Finally, the sensitivity of the remotely sensed total and polarized reflectance to the measured in-water optical properties was analyzed at the aircraft altitude and the TOA. Total and polarized values above and below the detection limits were highlighted for both elevations. Overall, the results demonstrated the ability to measure and model the remotely sensed polarized reflectance from airborne observations and the potential to provide additional information about aerosol and water constituents from airborne and space-borne polarimetric observations, such as particle size and type. This study clearly confirms that it remains important to continue the development of advanced ocean color retrieval algorithms based on the exploitation of multi-angular polarimetric remote sensing measurements for use in forthcoming satellite sensors such as the PACE sensors (NASA) or the Multidirectional, Multipolarization, and Multispectral (3MI) instrument (ESA and EUMETSAT).

Declaration of Competing Interest

None.

Acknowledgments

Funding for this work is provided by the Office of Naval Research (ONR). The research was performed while Dr. Ahmed El-Habashi held an NRC Research Associateship award at the U.S. Naval Research Laboratory in Washington, DC, under contractor number N00173-17-2-C002. We would like to thank the Centre National d'Etudes Spatiales (CNES-France) for the maintenance and the online distribution of the OSOAA radiative transfer model (<https://github.com/CNES/RadiativeTransferCode-OSOAA>). We acknowledge our thanks to the NASA AERONET staff and Dr. Brent Holben, site manager, for providing the aerosol properties used in part of the analysis. The satellite imagery in Fig. 1 was downloaded from the NASA Worldview (<https://worldview.earthdata.nasa.gov>). We would like to particularly thank Dr. Tanya C. Garza and Dr. Marcos J. Montes for their insightful remarks and the anonymous reviewers for their comments and suggestions, which significantly improved the quality of the manuscript.

Appendix

The square of the total uncertainties in Q and U , can be first derived analytically from the partial derivatives in Eq. (2) as follows:

$$\begin{bmatrix} u_Q^2 \\ u_U^2 \end{bmatrix} = \begin{bmatrix} \sigma_{I_0}^2 - \sigma_{I_0 I_{90}} - \sigma_{I_{90} I_0} + \sigma_{I_{90}}^2 \\ \sigma_{I_{45}}^2 - \sigma_{I_{45} I_{135}} - \sigma_{I_{135} I_{45}} + \sigma_{I_{135}}^2 \end{bmatrix}$$

Note that the uncertainty in the rotation angle (u_α) used with Q and U calculations is considered in all the uncertainty propagation calculations. However, the uncertainty formulations has been simplified in the article by ignoring the rotation angle uncertainty term ($\sigma_\alpha \ll$).

To estimate the total uncertainties in $DoLP$ and $AoLP$, we analytically compute the partial derivatives in Eq. (2). We start by calculating the partial derivatives in Eq. (3) for $DoLP$. The $DoLP$ partial derivatives can be simplified as follow:

$$\frac{\partial DoLP}{\partial I_0} = \frac{-U^2 - Q(I + 2I_{90})}{2I^2 \sqrt{Q^2 + U^2}}$$

$$\frac{\partial DoLP}{\partial I_{45}} = \frac{-Q^2 - U(I - 2I_{135})}{2I^2 \sqrt{Q^2 + U^2}},$$

$$\frac{\partial DoLP}{\partial I_{90}} = \frac{-U^2 - Q(I + 2I_0)}{2I^2 \sqrt{Q^2 + U^2}},$$

$$\frac{\partial DoLP}{\partial I_{135}} = \frac{-Q^2 - U(I + 2I_{45})}{2I^2 \sqrt{Q^2 + U^2}}$$

To obtain the total uncertainty of *DoLP*, we substitute the *DoLP* partial derivatives in Eq. (2). Thus, the u_{DoLP}^2 can be simplified as follow:

$$u_{DoLP}^2 = \frac{1}{I^2(Q^2 + U^2)} \left(\begin{aligned} & \left((U^2 + Q(I_{45} + 2I_{90} + I_{135})) \times (a_1\sigma_{I_0}^2 + a_2\sigma_{I_{45}I_0} + a_3\sigma_{I_{90}I_0} + a_4\sigma_{I_{135}I_0}) \right) \\ & + \left((Q^2 + U(I_0 + I_{90} - 2I_{135})) \times (a_1\sigma_{I_0I_{45}} + a_2\sigma_{I_{45}I_{90}} + a_3\sigma_{I_{90}I_{45}} + a_4\sigma_{I_{135}I_{45}}) \right) \\ & + \left((U^2 + Q(2I_0 + I_{45} + I_{135})) \times (a_1\sigma_{I_0I_{90}} + a_2\sigma_{I_{45}I_{90}} + a_3\sigma_{I_{90}I_{90}} + a_4\sigma_{I_{135}I_{90}}) \right) \\ & + \left((Q^2 + U(I_0 + 2I_{45} + I_{90})) \times (a_1\sigma_{I_0I_{135}} + a_2\sigma_{I_{45}I_{135}} + a_3\sigma_{I_{90}I_{135}} + a_4\sigma_{I_{135}I_{135}}) \right) \end{aligned} \right)$$

The coefficients a_1 , a_2 , a_3 , and a_4 are defined by

$$\begin{bmatrix} a_1 \\ a_2 \\ a_3 \\ a_4 \end{bmatrix} = \frac{1}{I^2(Q^2 + U^2)} \begin{bmatrix} U^2 + Q(I_{45} + 2I_{90} + I_{135}) \\ Q^2 + U(I_0 + I_{90} - 2I_{135}) \\ U^2 + Q(2I_0 + I_{45} + I_{135}) \\ Q^2 + U(I_0 + 2I_{45} + I_{90}) \end{bmatrix}$$

where $\sigma_{I_0}^2$, $\sigma_{I_{45}}^2$, $\sigma_{I_{90}}^2$, and $\sigma_{I_{135}}^2$ are the variances of each Stocks component, and $\sigma_{I_0I_{45}}$, $\sigma_{I_0I_{90}}$, and $\sigma_{I_0I_{135}}$ are the covariances between each of the Stocks components. All parameters above come from the imager measurements.

Similarly, we compute the total uncertainties in *AoLP* parameter. We start by calculating the partial derivatives in Eq. (2) for *AoLP*. The *AoLP* partial derivatives can be simplified as follows:

$$\frac{\partial AoLP}{\partial I_0} = -\frac{\partial AoLP}{\partial I_{90}} = \frac{-U}{Q^2 \left(\frac{2U^2}{Q^2} + 2 \right)},$$

$$\frac{\partial AoLP}{\partial I_{45}} = -\frac{\partial AoLP}{\partial I_{135}} = \frac{1}{Q \left(\frac{2U^2}{Q^2} + 2 \right)},$$

The u_{AoLP}^2 can be obtained by substituting the partial derivatives in Eq. (2) as follows:

$$u_{AoLP}^2 = \frac{1}{4Q^2 \left(\frac{2U^2}{Q^2} + 1 \right)^2} \times \left(\begin{aligned} & \left(\sigma_{I_{45}}^2 - \sigma_{I_{135}I_{45}} - \sigma_{I_{45}I_{135}} + \sigma_{I_{135}}^2 + \frac{U}{Q}(-\sigma_{I_0I_{45}} + \sigma_{I_{90}I_{45}} + \sigma_{I_0I_{135}} - \sigma_{I_{90}I_{135}}) \right) \\ & - \frac{U}{Q}(\sigma_{I_{45}I_0} - \sigma_{I_{135}I_0} + \sigma_{I_{45}I_{90}} - \sigma_{I_{135}I_{90}} + \frac{U}{Q}(-\sigma_{I_0}^2 + \sigma_{I_{90}I_0} - \sigma_{I_0I_{90}} + \sigma_{I_{90}}^2) \end{aligned} \right)$$

References

[1] Goyens C, Jamet C, Schroeder T. Evaluation of four atmospheric correction algorithms for MODIS-Aqua images over contrasted coastal waters. *Remote Sens Environ* 2013;131:63–75.

[2] Ibrahim A, Franz B, Ahmad Z, Healy R, Knobelspiesse K, Gao B-C, et al. Atmospheric correction for hyperspectral ocean color retrieval with application to the Hyperspectral Imager for the Coastal Ocean (HICO). *Remote Sens Environ* 2018;204:60–75.

[3] Hu C, Lee Z, Franz B. Chlorophyll algorithms for oligotrophic oceans: A novel approach based on three-band reflectance difference. *J Geophys Res Oceans* 2012;117.

[4] Werdell PJ, Franz BA, Bailey SW, Feldman GC, Boss E, Brando VE, et al. Generalized ocean color inversion model for retrieving marine inherent optical properties. *Appl Opt* 2013;52:2019–37.

[5] Werdell PJ, Franz BA, Lefler JT, Robinson WD, Boss E. Retrieving marine inherent optical properties from satellites using temperature and salinity-dependent backscattering by seawater. *Optics Express* 2013;21:32611–22.

[6] Gilerson A, Zhou J, Hlaing S, Ioannou I, Gross B, Moshary F, et al. Fluorescence component in the reflectance spectra from coastal waters. II. Performance of retrieval algorithms. *Optics Express* 2008;16:2446–60.

[7] Lee Z, Carder KL, Arnone RA. Deriving inherent optical properties from water color: a multiband quasi-analytical algorithm for optically deep waters. *Appl Opt* 2002;41:5755–72.

[8] Werdell PJ, Bailey SW. An improved in-situ bio-optical data set for ocean color algorithm development and satellite data product validation. *Remote Sens Environ* 2005;98:122–40.

[9] Gower JF, Brown L, Borstad G. Observation of chlorophyll fluorescence in west coast waters of Canada using the MODIS satellite sensor. *Can J Remote Sens* 2004;30:17–25.

[10] El-Habashi A, Ioannou I, Tomlinson M, Stumpf R, Ahmed S. Satellite retrievals of *Karenia brevis* harmful algal blooms in the west florida shelf using neural networks and comparisons with other techniques. *Rem Sensing* 2016;8:377.

[11] El-Habashi A, Duran CM, Lovko V, Tomlinson MC, Stumpf RP, Ahmed S. Satellite retrievals of *Karenia brevis* harmful algal blooms in the West Florida shelf using neural networks and impacts of temporal variabilities. *J Appl Remote Sens* 2017;11:032408.

[12] El-Habashi A, Ahmed S, Ondrusek ME, VJJoARS Lovko. Analyses of satellite ocean color retrievals show advantage of neural network approaches and algorithms that avoid deep blue bands. *J Appl Remote Sens* 2019;13:024509.

[13] Wang M, LJTToG Jiang, Sensing R. Atmospheric correction using the information from the short blue band. *IEEE Trans Geosci Remote Sens* 2018;56:6224–37.

[14] Chowdhary J, Cairns B, Waquet F, Knobelspiesse K, Ottaviani M, Redemann J, et al. Sensitivity of multiangle, multispectral polarimetric remote sensing over open oceans to water-leaving radiance: Analyses of RSP data acquired during the MILAGRO campaign. *Remote Sens Environ* 2012;118:284–308.

[15] Chami M. Importance of the polarization in the retrieval of oceanic constituents from the remote sensing reflectance. *J Geophys Res Oceans* 2007:112.

[16] Chami M, MDJJoGRO Patel. Sensitivity of the retrieval of the inherent optical properties of marine particles in coastal waters to the directional variations and the polarization of the reflectance. *J Geophys Res Oceans* 2007:112.

[17] Chowdhary J, Cairns B, Mishchenko M, Travis L. Retrieval of aerosol properties over the ocean using multispectral and multiangle photopolarimetric measurements from the Research Scanning Polarimeter. *Geophys Res Lett* 2001;28:243–6.

[18] Hansen JE, Travis LD. Light scattering in planetary atmospheres. *Space Sci Rev* 1974;16:527–610.

[19] Mishchenko MI, Travis LD, Lacis AA. Scattering, absorption, and emission of light by small particles. Cambridge University Press; 2002.

[20] Dubovik O, Li Z, Mishchenko MI, Tanré D, Karol Y, Bojkov B, et al. Polarimetric remote sensing of atmospheric aerosols: Instruments, methodologies, results, and perspectives. *J Quant Spectros Rad Transf* 2019;224:474–511.

[21] Stammes S, Hostetler C, Ferrare R, Burton S, Liu X, Hair J, et al. Simultaneous polarimeter retrievals of microphysical aerosol and ocean color parameters from the “MAPP” algorithm with comparison to high-spectral-resolution lidar aerosol and ocean products. *Appl Opt* 2018;57:2394–413.

[22] Knobelspiesse K, Cairns B, Mishchenko M, Chowdhary J, Tsigaridis K, van Diedenhoven B, et al. Analysis of fine-mode aerosol retrieval capabilities by different passive remote sensing instrument designs. *Optics Express* 2012;20:21457–84.

[23] Loisel H, Duforet L, Dessailly D, Chami M, PJOe Dubuisson. Investigation of the variations in the water leaving polarized reflectance from the POLDER satellite data over two biogeochemical contrasted oceanic areas. *Optics express* 2008;16:12905–18.

[24] Tonizzo A, Zhou J, Gilerson A, Twardowski MS, Gray DJ, Arnone RA, et al. Polarized light in coastal waters: hyperspectral and multiangular analysis. *Optics Express* 2009;17:5666–83.

[25] Bowles JH, Korwan DR, Montes MJ, Gray DJ, Gillis DB, Lamela GM, et al. Airborne system for multispectral, multiangle polarimetric imaging. *Appl Opt* 2015;54:F256–FF67.

[26] Hooper BA, Van Pelt B, Williams J, Dugan J, Yi M, Piotrowski C, et al. Airborne spectral polarimeter for ocean wave research. *J Atmos Ocean Tech* 2015;32:805–15.

[27] Chowdhary J, Zhai P-W, Xu F, Frouin R, DJJoQS Ramon, Transfer R. Testbed results for scalar and vector radiative transfer computations of light in atmosphere-ocean systems. *J Quant Spectros Rad Transf* 2020;242:106717.

[28] Mishchenko MI, Cairns B, Hansen JE, Travis LD, Burg R, Kaufman YJ, et al. Monitoring of aerosol forcing of climate from space: analysis of measurement requirements. *J Quant Spectros Rad Transf* 2004;88:149–61.

[29] Kattawar GW. Genesis and evolution of polarization of light in the ocean. *Appl Opt* 2013;52:940–8.

[30] Jamet C, Ibrahim A, Ahmad Z, Angelini F, Babin M, Behrenfeld MJ, et al. Going beyond standard ocean color observations: lidar and polarimetry. *Front Earth Sci* 2019;6:251.

[31] Werdell PJ, McKinna LI, Boss E, Ackleson SG, Craig SE, Gregg WW, et al. An overview of approaches and challenges for retrieving marine inherent optical properties from ocean color remote sensing. *Progress Ocean* 2018;160:186–212.

[32] Deschamps P-Y, Bréon F-M, Leroy M, Podaire A, Bricaud A, Buriez J-C, et al. The POLDER mission: Instrument characteristics and scientific objectives. *IEEE Trans Geosci Remote Sens* 1994;32:598–615.

[33] Fournier B, Bracco G, Lafrance B, Ruffel C, Hagolle O, Tinel C. PARASOL in-flight calibration and performance. *Appl Opt* 2007;46:5435–51.

[34] Deuzé J, Bréon F, Devaux C, Goloub P, Herman M, Lafrance B, et al. Remote sensing of aerosols over land surfaces from POLDER-ADEOS-1 polarized measurements. *J Geophys Res Atmos* 2001;106:4913–26.

[35] Tanré D, Bréon F, Deuzé J, Dubovik O, Ducos F, François P, et al. Remote sensing of aerosols by using polarized, directional and spectral measurements within the A-Train: the PARASOL mission. *Atmos Meas Tech* 2011;4:2037–69.

[36] Mishchenko MI, Cairns B, Kopp G, Schueler CF, Fafaul BA, Hansen JE, et al. Accurate monitoring of terrestrial aerosols and total solar irradiance: introducing the Glory Mission. *Bull Am Meteorol Soc* 2007;88:677–92.

- [37] PeraltaRJ, NardelliC, CairnsB, RussellEE, TravisLD, MishchenkoMI, et al. Aerosol polarimetry sensor for the Glory Mission. MIPPR 2007: Automatic Target Recognition and Image Analysis; and Multispectral Image Acquisition: International Society for Optics and Photonics; 2007. p. 67865L.
- [38] Imaoka K, Kachi M, Fujii H, Murakami H, Hori M, Ono A, et al. Global Change Observation Mission (GCOM) for monitoring carbon, water cycles, and climate change. *Proc IEEE* 2010;98:717–34.
- [39] Junjie G, Zhigang YJRST. Application. Airborne experiment of TG-2 multi-angle polarization imager for cloud phase identification. *Remote Sensing Technology and Application* 2018;33:439–48.
- [40] Chen X, Wang J, Liu Y, Xu X, Cai Z, Yang D, et al. Angular dependence of aerosol information content in CAP/TanSat observation over land: Effect of polarization and synergy with A-train satellites. *Remote Sens Environ* 2017;196:163–77.
- [41] Li Z, Hou W, Hong J, Zheng F, Luo D, Wang J, et al. Directional Polarimetric Camera (DPC): Monitoring aerosol spectral optical properties over land from satellite observation. *J Quant Spectros Rad Transf* 2018;218:21–37.
- [42] Diner DJ, Beckert JC, Reilly TH, Bruegge CJ, Conel JE, Kahn RA, et al. Multi-angle Imaging SpectroRadiometer (MISR) instrument description and experiment overview. *IEEE Trans Geosci Remote Sens* 1998;36:1072–87.
- [43] Liu Y, Diner DJPHR. Multi-angle imager for aerosols: a satellite investigation to benefit public health. *Public Health Reports* 2017;132:14–17.
- [44] Diner DJ, Boland SW, Brauer M, Bruegge C, Burke KA, Chipman R, et al. Advances in multiangle satellite remote sensing of speciated airborne particulate matter and association with adverse health effects: from MISR to MAIA. *J Appl Remote Sens* 2018;12:042603.
- [45] Cetinic I, McClain CR, Werdell PJ, Ahmad Z, Ahmad Z, Arnore R, et al. PACE Technical Report Series, 7. Ocean Color Instrument (OCI) Concept Design Studies; 2018.
- [46] Cetinic I, McClain CR, Series Werdell PJPACE Technical Report, 3 Volume. Polarimetry in the PACE Mission: Science Team Consensus Document; 2018.
- [47] Antoine D, Juergen F, Fougne B, Remer LA, Remer L, Knobelspiesse K, et al. Retrieving aerosol characteristics from the PACE mission, Part 2: multi-angle and polarimetry. From the Satellite to the Earth's Surface: Studies Relevant to NASA's Plankton, Aerosol, Cloud, Ocean Ecosystems (PACE) Mission; 2020.
- [48] Werdell PJ, Behrenfeld MJ, Bontempi PS, Boss E, Cairns B, Davis GT, et al. The Plankton, Aerosol, Cloud, ocean Ecosystem mission: status, science, advances. *Bull Am Meteorol Soc* 2019;100:1775–94.
- [49] Fernandez Borda R, Martins J, McBride B, Remer L, Barbosa HJA. Capabilities of the HARP2 Polarimetric Sensor on the PACE Satellite. *AGUFM* 2018;2018 OS11D-1431.
- [50] Hasekamp OP, Fu G, Rusli SP, Wu L, Di Noia A, aan de Brugh J, et al. Aerosol measurements by SPEXone on the NASA PACE mission: expected retrieval capabilities. *J Quant Spectros Rad Transf* 2019;227:170–84.
- [51] Fougne B, Marbach T, Lacan A, Lang R, Schlüssel P, Poli G, et al. The multi-viewing multi-channel multi-polarisation imager—overview of the 3MI polarimetric mission for aerosol and cloud characterization. *J Quant Spectros Rad Transf* 2018;219:23–32.
- [52] Milinevsky G, Yatskiv Y, Degtyaryov O, Syniavskiy I, Mishchenko M, Rosenbush V, et al. New satellite project Aerosol-UA: Remote sensing of aerosols in the terrestrial atmosphere. *Acta Astronautica* 2016;123:292–300.
- [53] Waquet F, Léon JF, Goloub P, Pelon J, Tanré D, JJJJoGRA Deuzé. Maritime and dust aerosol retrieval from polarized and multispectral active and passive sensors. *J Geophys Res Atmos* 2005;110.
- [54] Waquet F, Goloub P, Deuzé JL, Léon JF, Auriol F, Verwaerde C, et al. Aerosol retrieval over land using a multiband polarimeter and comparison with path radiance method. *J Geophys Res Atmos* 2007;112.
- [55] Waquet F, Léon J-F, Cairns B, Goloub P, Deuzé J-L, Auriol FJAO. Analysis of the spectral and angular response of the vegetated surface polarization for the purpose of aerosol remote sensing over land. *Appl Opt* 2009;48:1228–36.
- [56] Auriol F, Léon J-F, Balois J-Y, Verwaerde C, François P, Riedi J, et al. Multidirectional visible and shortwave infrared polarimeter for atmospheric aerosol and cloud observation: OSIRIS (Observing System Including Polarisation in the Solar Infrared Spectrum). *Multispectral, Hyperspectral, and Ultraspectral Remote Sensing Technology, Techniques, and Applications II*. International Society for Optics and Photonics; 2008. 71491D.
- [57] Cairns B, Russell EE, LaVeigne JD, Tennant PM. Research scanning polarimeter and airborne usage for remote sensing of aerosols. *Polar Sci Remote Sens Int Soc Opt Photon* 2003;33–44.
- [58] Chowdhary J, Cairns B, Mishchenko MI, Hobbs PV, Cota GF, Redemann J, et al. Retrieval of aerosol scattering and absorption properties from photopolarimetric observations over the ocean during the CLAMS experiment. *J Atmos Sci* 2005;62:1093–117.
- [59] Alexandrov MD, Cairns B, Sinclair K, Wasilewski AP, Ziemba L, Crosbie E, et al. Retrievals of cloud droplet size from the research scanning polarimeter data: Validation using in situ measurements. *Remote Sens Environ* 2018;210:76–95.
- [60] Diner D, Xu F, Garay M, Martonchik J, Rheingans B, Geier S, et al. The Airborne Multiangle SpectroPolarimetric Imager (AirMSPi): a new tool for aerosol and cloud remote sensing. *Atmos Measure Tech* 2013;6:2007.
- [61] Xu F, Dubovik O, Zhai P-W, Diner DJ, Kalashnikova OV, Seidel FC, et al. Joint retrieval of aerosol and water-leaving radiance from multispectral, multiangular and polarimetric measurements over ocean. *Meas Tech* 2016;9:2877–907.
- [62] Xu F, van Harten G, Diner DJ, Kalashnikova OV, Seidel FC, Bruegge CJ, et al. Coupled retrieval of aerosol properties and land surface reflection using the Airborne Multiangle SpectroPolarimetric Imager. *J Geophys Res Atmos* 2017;122:7004–26.
- [63] Xu F, van Harten G, Diner DJ, Davis AB, Seidel FC, Rheingans B, et al. Coupled Retrieval of Liquid Water Cloud and Above-Cloud Aerosol Properties Using the Airborne Multiangle SpectroPolarimetric Imager (AirMSPi). *J Geophys Res Atmos* 2018;123:3175–204.
- [64] Fu G, Hasekamp O, Rietjens J, Smit M, Noia AD, Cairns B, et al. Aerosol retrievals from different polarimeters during the ACEPOL campaign using a common retrieval algorithm. *Atmos Measure Tech* 2020;13:553–73.
- [65] Smit JM, Rietjens JH, van Harten G, Di Noia A, Laauwen W, Rheingans BE, et al. SPEX airborne spectropolarimeter calibration and performance. *Appl Opt* 2019;58:5695–719.
- [66] BJToG Fougne, Sensing R. Improvement of the PARASOL radiometric in-flight calibration based on synergy between various methods using natural targets. *IEEE Trans Geosci Remote Sens* 2015;54:2140–52.
- [67] Marbach T, Riedi J, Lacan A, Schlüssel P. The 3MI mission: multi-viewing-channel-polarisation imager of the EUMETSAT polar system: second generation (EPS-SG) dedicated to aerosol and cloud monitoring. *Polar Sci Remote Sens VII Int Soc Opt Photon* 2015:961310.
- [68] Gao M, Zhai P-W, Franz B, Hu Y, Knobelspiesse K, Werdell PJ, et al. Inversion of multi-angular polarimetric measurements over open and coastal ocean waters: a joint retrieval algorithm for aerosol and water leaving radiance properties. *Atmos Measure Tech* 2019.
- [69] Hasekamp OP, Litvinov P, AJJoGRA Butz. Aerosol properties over the ocean from PARASOL multiangle photopolarimetric measurements. *J Geophys Res Atmos* 2011;116.
- [70] Chowdhary J, Cairns B, Travis LD. Contribution of water-leaving radiances to multiangle, multispectral polarimetric observations over the open ocean: bio-optical model results for case 1 waters. *Appl Opt* 2006;45:5542–5567.
- [71] Tonizzo A, Gilerson A, Harmel T, Ibrahim A, Chowdhary J, Gross B, et al. Estimating particle composition and size distribution from polarized water-leaving radiance. *Appl Opt* 2011;50:5047–58.
- [72] El-Habashi A, Ahmed S. Chlorophyll fluorescence and the polarized underwater light field: comparison of vector radiative transfer simulations and multi-angular hyperspectral polarization field measurements. *SPIE Defense+ Security*. International Society for Optics and Photonics; 2016. 98270U-U-15.
- [73] Harmel T, Gilerson A, Hlaing S, Weidemann A, Arnore R, Ahmed S. Long Island Sound Coastal Observatory: assessment of above-water radiometric measurement uncertainties using collocated multi and hyper-spectral systems: reply to comment. *Appl Opt* 2012;51:3893–9.
- [74] Ibrahim A, Gilerson A, Chowdhary J, Ahmed S. Retrieval of macro-and micro-physical properties of oceanic hydrosols from polarimetric observations. *Remote Sens Environ* 2016;186:548–66.
- [75] Zhai P-W, Knobelspiesse K, Ibrahim A, Franz BA, Hu Y, Gao M, et al. Water-leaving contribution to polarized radiation field over ocean. *Optics Express* 2017;25:A689–708.
- [76] El-Habashi A. Remote sensing over coastal and open oceans: Retrieval of water constituents from scalar and polarimetric observations. ProQuest: The City College of the City University of New York; 2018.
- [77] Gilerson A, Carrizo C, Ibrahim A, Foster R, Harmel T, El-Habashi A, et al. Hyperspectral polarimetric imaging of the water surface and retrieval of water optical parameters from multi-angular polarimetric data. *Appl Opt* 2020;59:C8–C20.
- [78] Gao M, Zhai P-W, Franz BA, Knobelspiesse K, Ibrahim A, Cairns B, et al. Inversion of multi-angular polarimetric measurements from the ACEPOL campaign: an application of improving aerosol property and hyperspectral ocean color retrievals. UMBC Faculty Collection; 2020.
- [79] Koestner D, Stramski D, Reynolds RJQSRT. Polarized light scattering measurements as a means to characterize particle size. *Appl Opt* 2012;113:565–74.
- [80] Koestner D, Stramski D, Reynolds RAJO. Polarized light scattering measurements as a means to characterize particle size and composition of natural assemblages of marine particles. *Appl Opt* 2020;59:8314–34.
- [81] Foster R, Gilerson A. Polarized transfer functions of the ocean surface for above-surface determination of the vector submarine light field. *Appl Opt* 2016;55:9476–94.
- [82] Roesler CS, AHJMio Barnard. Optical proxy for phytoplankton biomass in the absence of photophysiology: Rethinking the absorption line height. *Method Ocean* 2013;7:79–94.
- [83] Gould RW, Stavn RH, Twardowski MS, Lamela G. Partitioning optical properties into organic and inorganic components from ocean color imagery. *Naval Res Lab Stennis Space Center MS Ocean Div*; 2002.
- [84] Stramski D, Li L, RAJO Reynolds. Model for separating the contributions of non-algal particles and colored dissolved organic matter to light absorption by seawater. *Appl Opt* 2019;58:3790–806.
- [85] Holben BN, Eck TF, la Slutsker, Tanre D, Buis J, Setzer A, et al. AERONET—A federated instrument network and data archive for aerosol characterization. *Remote Sens Environ* 1998;66:1–16.
- [86] Lee J, Kim J, Song C, Kim S, Chun Y, Sohn B, et al. Characteristics of aerosol types from AERONET sunphotometer measurements. *Atmos Environ* 2010;44:3110–17.
- [87] BIPM I, IFCC I, ISO IUAPAOIML. Evaluation of Measurement Data—Guide to the Expression of Uncertainty in Measurement. Joint Committee for Guides in Metrology. JCGM 2008.
- [88] Knobelspiesse K, Tan Q, Bruegge C, Cairns B, Chowdhary J, van Diedenhoven B, et al. Intercomparison of airborne multi-angle polarimeter obser-

- variations from the Polarimeter Definition Experiment. *Appl Opt* 2019;58:650–669.
- [89] McKinna L, Cetinic I, Chase A, JFiES Werdell. Approach for propagating radiometric data uncertainties through NASA ocean color algorithms. *Front Earth Sci* 2019;7:176.
- [90] Pahlevan N, Sarkar S, BJRSoE Franz. Uncertainties in coastal ocean color products: Impacts of spatial sampling. *Remote Sens Environ* 2016;181:14–26.
- [91] Taylor J. Statistical analysis of random uncertainties. *An Introduction to Error Analysis: Univ. Science Books*; 1997.
- [92] Lee Z, Arnone R, Hu C, Werdell PJ, Lubac BJAo. Uncertainties of optical parameters and their propagations in an analytical ocean color inversion algorithm. *Appl Opt* 2010;49:369–81.
- [93] Qi L, Lee Z, Hu C, MjJoGRO Wang. Requirement of minimal signal-to-noise ratios of ocean color sensors and uncertainties of ocean color products. *J Geophys Res Oceans* 2017;122:2595–611.
- [94] Meister G. The first SIMBIOS radiometric intercomparison (SIMRIC-1), april–september 2001. National Aeronautics and Space Administration, Goddard Space Flight Center; 2002.
- [95] Foster R. The polarization of light in coastal and open oceans: Reflection and transmission by the air–sea interface and application for the retrieval of water optical properties. The City College of New York; 2017.
- [96] Fraser RS, Mattoo S, Yeh EN, CjJoGRA McClain. Algorithm for atmospheric and glint corrections of satellite measurements of ocean pigment. *J Geophys Res Atmos* 1997;102:17107–18.
- [97] Gao B-C, Montes MJ, Ahmad Z, COJAo Davis. Atmospheric correction algorithm for hyperspectral remote sensing of ocean color from space. *Appl Opt* 2000;39:887–96.
- [98] Frouin RJ, Franz BA, Ibrahim A, Knobelspiesse KD, Ahmad Z, Cairns B, et al. Atmospheric correction of satellite ocean-color imagery during the PACE era. *Front Earth Sci* 2019.
- [99] Dierssen HMJES. Hyperspectral measurements, parameterizations, and atmospheric correction of whitecaps and foam from visible to shortwave infrared for ocean color remote sensing. *Front Earth Sci* 2019;7:14.
- [100] Deuzé J-L, Herman M, RjJoQS Santer, Transfer R. Fourier series expansion of the transfer equation in the atmosphere–ocean system. *J Quant Spectros Rad Transf* 1989;41:483–94.
- [101] Lenoble J, Herman M, Deuzé J, Lafrance B, Santer R, DjJoQS Tanré, et al. A successive order of scattering code for solving the vector equation of transfer in the earth's atmosphere with aerosols. *J Quant Spectros Rad Transf* 2007;107:479–507.
- [102] Chami M, Lafrance B, Fougne B, Chowdhary J, Harmel T, FJOe Waquet. OSOAA: a vector radiative transfer model of coupled atmosphere–ocean system for a rough sea surface application to the estimates of the directional variations of the water leaving reflectance to better process multi-angular satellite sensors data over the ocean. *Optics Express* 2015;23:27829–52.
- [103] JJoP Orphal, Chemistry PA. A critical review of the absorption cross-sections of O₃ and NO₂ in the ultraviolet and visible. *J Photochem Photobiol A Chem* 2003;157:185–209.
- [104] Chehade W, Gür B, Spietz P, Gorshelev V, Serdyuchenko A, Burrows J, et al. Temperature dependent ozone absorption cross section spectra measured with the GOME-2 FM3 spectrometer and first application in satellite retrievals. *Atmos Measure Tech* 2013;6:1623.
- [105] Tanre D, Herman M, Deschamps P, De Lefle AJAo. Atmospheric modeling for space measurements of ground reflectances, including bidirectional properties. *Appl Opt* 1979;18:3587–94.
- [106] Platt T. Why ocean colour?: The societal benefits of ocean-colour technology. International Ocean–Colour Coordinating Group; 2008.
- [107] Harmel T, Gilerson A, Hlaing S, Tonizzo A, Legbandt T, Weidemann A, et al. Long Island Sound Coastal Observatory: assessment of above-water radiometric measurement uncertainties using collocated multi and hyperspectral systems. *Appl Opt* 2011;50:5842–60.
- [108] Cox C, Munk WJJ. Measurement of the roughness of the sea surface from photographs of the sun's glitter. *Josa* 1954;44:838–50.
- [109] Chowdhary J, Zhai P, Boss E, Dierssen HM, Frouin RJ, Ibrahim AI, et al. Modeling atmosphere–ocean radiative transfer: A PACE mission perspective. *Front Earth Sci* 2019;7:100.
- [110] Mobley CD, Sundman LK, EJAo Boss. Phase function effects on oceanic light fields. *Appl Opt* 2002;41:1035–50.
- [111] Sullivan JM, Twardowski MSJAo. Angular shape of the oceanic particulate volume scattering function in the backward direction. *Appl Opt* 2009;48:6811–19.
- [112] Twardowski MS, Boss E, Macdonald JB, Pegau WS, Barnard AH, JRVJJoGRO Zaneveld. A model for estimating bulk refractive index from the optical backscattering ratio and the implications for understanding particle composition in case I and case II waters. *J Geophys Res Oceans* 2001;106:14129–42.
- [113] Boss E, Twardowski MS, Herring S. Shape of the particulate beam attenuation spectrum and its inversion to obtain the shape of the particulate size distribution. *Appl Opt* 2001;40:4885–93.
- [114] Farinato RS, RLJJoCP Rowell. New values of the light scattering depolarization and anisotropy of water. *J Chem Phys* 1976;65:593–5.
- [115] Zhang X, Stramski D, Reynolds RA, ERJAo Blocker. Light scattering by pure water and seawater: the depolarization ratio and its variation with salinity. *Appl Opt* 2019;58:991–1004.
- [116] Thuillier G, Hersé M, Foujols T, Peetermans W, Gillotay D, Simon P, et al. The solar spectral irradiance from 200 to 2400 nm as measured by the SOLSPEC spectrometer from the ATLAS and EURECA missions. *Solar Phys* 2003;214:1–22.
- [117] Ottaviani M, Foster R, Gilerson A, Ibrahim A, Carrizo C, El-Habashi A, et al. Airborne and shipborne polarimetric measurements over open ocean and coastal waters: intercomparisons and implications for spaceborne observations. *Remote Sens Environ* 2018;206:375–90.
- [118] Pust NJ, Dahlberg AR, Thomas MJ, JAJOe Shaw. Comparison of full-sky polarization and radiance observations to radiative transfer simulations which employ AERONET products. *Optics Express* 2011;19:18602–13.
- [119] Emde C, Barlakas V, Cornet C, Evans F, Korkin S, Ota Y, et al. IPRT polarized radiative transfer model intercomparison project–Phase A. *J Quant Spectros Rad Transf* 2015;164:8–36.
- [120] Lu Y, Zhou Y, Liu Y, Mao Z, Qian W, Wang M, et al. Using remote sensing to detect the polarized sunglint reflected from oil slicks beyond the critical angle. *J Geophys Res* 2017;122:6342–54.
- [121] Ottaviani M, Chowdhary J, BJRSoE Cairns. Remote sensing of the ocean surface refractive index via short-wave infrared polarimetry. *Remote Sens Environ* 2019;221:14–23.
- [122] Adams JT, GWJAo Kattawar. Neutral points in an atmosphere–ocean system. 1: Upwelling light field. *Appl Opt* 1997;36:1976–86.
- [123] Adams JT, Gray DJ, Rayner S. Observation of non-principal plane neutral points in the upwelling polarized light field above a water surface. *Appl Opt* 2012;51:5387–91.
- [124] Alexandrov MD, Cairns B, MjJoQS Mishchenko, Transfer R. Rainbow fourier transform. *J Quant Spectros Rad Transf* 2012;113:2521–35.
- [125] Voss KJ, Gleason AC, Gordon HR, Kattawar GW, You Y. Observation of non-principal plane neutral points in the in-water upwelling polarized light field. *Optics Express* 2011;19:5942–52.
- [126] Gleason AC, Voss KJ, Gordon HR, Twardowski MS, Berthon J-FJAS. Measuring and modeling the polarized upwelling radiance distribution in clear and coastal waters. *Appl Sci* 2018;8:2683.
- [127] Harmel T, Chami MJOE. Invariance of polarized reflectance measured at the top of atmosphere by PARASOL satellite instrument in the visible range with marine constituents in open ocean waters. *Optics Express* 2008;16:6064–80.